CrossMark

Compact high order finite volume method on unstructured grids II: Extension to two-dimensional Euler equations

Qian Wang [a], Yu-Xin Ren [a,*], Wanai Li [b]

[a] *Department of Engineering Mechanics, Tsinghua University, Beijing 100084, China*
[b] *Sino-French Institute of Nuclear Engineering & Technology, Sun Yat-Sen University, Zhuhai 519082, China*

ARTICLE INFO

ABSTRACT

In this paper, the compact least-squares finite volume method on unstructured grids proposed in our previous paper is extended to multi-dimensional systems, namely the two-dimensional Euler equations. The key element of this scheme is the compact least-squares reconstruction in which a set of constitutive relations are constructed by requiring the reconstruction polynomial and its spatial derivatives on the control volume of interest to conserve their averages on the face-neighboring cells. These relations result in an over-determined linear equation system. A large sparse system of linear equations is resulted by using the least-squares technique. An efficient solution strategy is of crucial importance for the application of the proposed scheme in multi-dimensional problems since both direct and iterative solvers for this system are computationally very expensive. In the present paper, it is found that in the cases of steady flow simulation and unsteady flow simulation using dual time stepping technique, the present reconstruction method can be coupled with temporal discretization scheme to achieve high computational efficiency. The WBAP limiter and a problem-independent shock detector are used in the simulation of flow with discontinuities. Numerical results demonstrate the high order accuracy, high computational efficiency and capability of handling both complex physics and geometries of the proposed schemes.

© 2016 Elsevier Inc. All rights reserved.

1. Introduction

A compact high order finite volume method on unstructured grids, termed as the compact least-squares finite volume (CLSFV) method, has been recently developed by Wang et al. [1] for solving one-dimensional conservation laws. In the present paper, the CLSFV method is extended to solve multi-dimensional Euler equations. Over the last two decades, various high order methods with compact stencils on unstructured grids have been developed, such as the discontinuous Galerkin (DG) method [2–6], $P_N P_M$ procedure [7–9], RDG method [10], DG/FV method [11,12], Residual Distribution (RD) method [13–16], spectral volume (SV) [17–20]/spectral difference (SD) [21–23] methods and correction procedure via reconstruction (CPR) method [24,25]. A common feature of these methods is that they can achieve high order accuracy on a compact stencil involving only face-neighboring cells (the von Neumann neighbors). This is the fundamental advantage of these methods over the high order finite volume (FV) methods, such as the *k*-exact [26–29]/WENO [30–33] FV methods, which require large stencils to reconstruct high order polynomial distributions within a typical control volume. The CLSFV method is an

improvement of the traditional FV schemes, which, similar to the DG, SV, SD and CPR methods, can achieve arbitrary high order accuracy using a compact stencil consisting of von Neumann neighbors. Unlike other compact finite volume schemes [34–36], the CLSFV method is intended to be applied on the unstructured grids.

The key element of the CLSFV method is the compact least-squares (CLS) reconstruction. The polynomial of a traditional reconstruction procedure in a FV scheme is determined by conserving the cell averages of the solution on the current cell as well as on the neighboring cells belonging to the stencil of the reconstruction for sufficiently smooth solution. Since the number of unknowns in the reconstruction polynomial increases very fast with the degree of the polynomial, a very large stencil is required for high order polynomial reconstruction. To cure this shortcoming and maintain the compact stencil for arbitrarily high order reconstruction, the CLS reconstruction procedure requires not only the dependent variables but also its various orders of derivatives to conserve their means on the control volumes belonging to a compact stencil consisting of only the face-neighboring cells. The conservation of the averages of the various orders of derivatives provides additional constitutive relations so that the reconstruction can be performed on a compact stencil. In practice, the number of all the constitutive relations is always larger than the unknowns in the reconstruction polynomial. Therefore, the constitutive relations result in an over-determined linear equation system, which, in the sense of least-squares, can be reduced to a block-tridiagonal linear equation system in one-dimensional cases. The block-tridiagonal linear solver can be used to solve the reconstruction problem directly [1].

However, in multi-dimensional cases, the CLS reconstruction generates a large sparse system of linear equations for which both direct and iterative solvers are computationally very expensive. Therefore, it is of crucial importance to design an efficient solution procedure. In this paper, it will be shown that the present scheme can be very efficient if an iterative solver for the CLS reconstruction is coupled properly with the time integration procedure. More specifically, for steady flow simulation, the iteration can be performed only once in every time step and the CLS reconstruction reaches its convergence only when the solution converges to steady state. The same idea can be also applied in unsteady flow simulation when dual time stepping technique is used in the implicit temporal discretization schemes. The dual time stepping technique can be considered as solving a modified steady problem by advancing in pseudo time at each physical time step. Thus in every pseudo time step, the iteration in the CLS reconstruction can be also performed only once. In summary, the iteration in the CLS reconstruction procedure does not need to reach full convergence when coupled with time integration in steady flow simulation or the pseudo time integration in the unsteady flow simulation where the temporal accuracy will not affect the converged solutions. Since the computation cost of one iteration step in the CLS reconstruction is very close to one k-exact reconstruction procedure, the coupled reconstruction/time integration procedure is as efficient as traditional FV schemes using k-exact reconstruction. Moreover, the numerical results of this paper indicate that the CLS reconstruction is usually more accurate than the k-exact reconstruction. As a result, the FV scheme using CLS reconstruction is generally more efficient than the traditional FV schemes using k-exact reconstruction in terms of the CPU time to reach the same accuracy. Therefore, the FV scheme using CLS reconstruction represents a viable approach in designing high order numerical schemes on unstructured grids using compact stencils.

The remainder of this paper is organized as follows. Section 2 presents the CLSFV method for solving multi-dimensional Euler equations. The framework of high order FV method is firstly introduced. Then the basic formulations of the multi-dimensional CLS reconstruction are presented in detail. An implicit reconstruction and implicit time integration coupled iteration method to achieve high computational efficiency is also presented. Other implementation details including the boundary treatment in the CLS reconstruction, the shock detector and the WBAP limiter are introduced in the section as well. The numerical examples are presented in Section 3 to validate the performance of the CLSFV method and the concluding remarks are given in Section 4.

2. High order compact least-squares FV method for 2D Euler equations

2.1. General framework of the high order finite volume schemes

This subsection describes the general framework for the high order cell-centered FV schemes on unstructured grids. The governing equations are the two-dimensional Euler equations in conservative form

$$\frac{\partial \mathbf{U}}{\partial t} + \frac{\partial \mathbf{F}}{\partial x} + \frac{\partial \mathbf{G}}{\partial y} = 0, \tag{1}$$

where $\mathbf{U}$ is the vector of conservative variables, $\mathbf{F}$ and $\mathbf{G}$ are the inviscid flux vectors defined by

$$\mathbf{U} = \begin{pmatrix} \rho \\ \rho u \\ \rho v \\ \rho E \end{pmatrix}, \qquad \mathbf{F} = \begin{pmatrix} \rho u \\ \rho u^2 + p \\ \rho u v \\ u(E + p) \end{pmatrix}, \qquad \mathbf{G} = \begin{pmatrix} \rho v \\ \rho u v \\ \rho v^2 + p \\ v(E + p) \end{pmatrix},$$

where ρ is the density, u and v are the velocity components in x and y directions, and p is the pressure. The total energy E is computed by

$$E = \frac{p}{\gamma - 1} + \frac{1}{2}\rho(u^2 + v^2), \quad \gamma = 1.4.$$
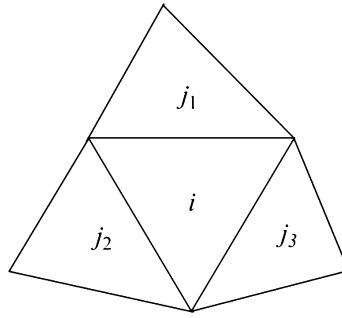
Fig. 1. Reconstruction stencil for cell i.

In this paper, we are interested in the FV schemes on triangular meshes. The computational domain Ω is partitioned into N non-overlapping triangular control volumes, i.e.,

$$\Omega = \bigcup_{i=1}^{N} \Omega_i.$$

The FV balance equations for control volume Ω_i is obtained by integrating Eq. (1) over the control volume and is expressed as

$$\frac{\partial}{\partial t} \int_{\Omega_i} \mathbf{U}_i dx dy + \oint_{\partial \Omega_i} \mathbf{f} \cdot \mathbf{n} dl = 0, \tag{2}$$

where $\partial \Omega_i$ is the boundary of Ω_i, $\mathbf{n} = (n_x, n_y)^{\mathrm{T}}$ is the outward unit vector normal to the surface $\partial \Omega_i$ and $\mathbf{f} = (\mathbf{F}, \mathbf{G})^{\mathrm{T}}$. For a triangular cell, $\partial \Omega_i = \bigcup_{m=1}^{3} I_m$, where I_m is the m-th side or interface of Ω_i. Therefore, Eq. (2) can be rewritten in the semi-discrete form as

$$\frac{\partial \overline{\mathbf{U}}_i}{\partial t} = -\frac{1}{\overline{\Omega}_i} \sum_{m=1}^{3} \int_{I_m} \mathbf{f} \cdot \mathbf{n} dl, \tag{3}$$

where $\overline{\mathbf{U}}_i = \frac{1}{\overline{\Omega}_i} \iint_{\Omega_i} \mathbf{U}_i dx dy$ is the cell average of the conservative variables and $\overline{\Omega}_i = \iint_{\Omega_i} dx dy$ is the cell volume.

The numerical fluxes in Eq. (3) are computed using the Gauss quadrature formula

$$\int_{I_m} \mathbf{f} \cdot \mathbf{n} dl \approx \left[\sum_{\varphi=1}^{NG} \omega_\varphi \mathbf{f}\big(\mathbf{U}(\mathbf{x}_{m,\varphi})\big) \right] \cdot \mathbf{n}_m \Delta l_m,$$

where NG is the number of Gaussian points. The flux function $\mathbf{f}(\mathbf{U}(\mathbf{x}_{m,\varphi}))$ is evaluated using the exact or approximate Riemann solvers or other flux splitting procedures, i.e.,

$$\mathbf{f}\big(\mathbf{U}(\mathbf{x}_{m,\varphi})\big) \cdot \mathbf{n}_m = \widetilde{\mathbf{f}}\big(\mathbf{U}^L(\mathbf{x}_{m,\varphi}), \mathbf{U}^R(\mathbf{x}_{m,\varphi}), \mathbf{n}_m\big)$$

where the left and right states $\mathbf{U}^L(\mathbf{x}_{m,\varphi}), \mathbf{U}^R(\mathbf{x}_{m,\varphi})$ are computed by the reconstructed distributions of the conservative variables. The high order CLS reconstruction will be described in Section 2.2. The approximate Riemann solver used in this paper is the standard Roe Riemann solver [37] using the entropy fix of Sanders et al. [38].

The spatially discretized semi-discrete FV scheme leads to a system of ordinary differential equations (ODEs)

$$\frac{d\overline{\mathbf{U}}}{dt} = \mathbf{R}(\mathbf{U}), \tag{4}$$

where $\mathbf{R}$ is the discrete form of the right hand side of Eq. (3). The ODEs need to be integrated in time to update the cell averages. The time integration scheme used in this paper will be described in Section 2.3.

2.2. High order compact least-squares reconstruction

This subsection presents the multi-dimensional CLS reconstruction. For arbitrarily high order CLS reconstruction, the stencil is always compact involving only face-neighboring cells denoted by $S_i = \{\Omega_{j_1}, \Omega_{j_2}, \Omega_{j_3}\}$ shown in Fig. 1.

Since the components of the conservative variables $\mathbf{U}$ are reconstructed separately, only a component of the conservative variables denoted by $u(\mathbf{x})$ is considered in this section.

The reconstruction problem in the FV scheme can be stated as follows. Given the cell average

$$\bar{u}_j = \frac{1}{\overline{\Omega}_j} \iint\limits_{\Omega_j} u(\mathbf{x})dxdy \tag{5}$$

of a solution $u(\mathbf{x})$ on every control volume $\Omega_j \in \Omega$, a degree k polynomial

$$u_i(\mathbf{x}) = \bar{u}_i + \sum_{l=1}^{DOF(k)} u_i^l \varphi_{l,i}(\mathbf{x}) \tag{6}$$

is constructed to approximate the solution on $\Omega_i \in \Omega$, where $DOF(k)$ is the number of the unknown coefficients in the polynomial, i.e., $DOF(k) = (k+1)(k+2)/2 - 1$ in two-dimensional cases. u_i^l is the unknown coefficient and $\varphi_{l,i}(\mathbf{x})$ is the zero-mean basis defined by

$$\varphi_{l,i}(\mathbf{x}) = \delta x_i^m \delta y_i^n - \overline{\delta x_i^m \delta y_i^n}$$

$$\delta x_i = (x - x_i)/h_i, \qquad \delta y_i = (y - y_i)/h_i, \qquad \overline{\delta x_i^m \delta y_i^n} = \frac{1}{\overline{\Omega}_i} \iint\limits_{\Omega_i} \delta x_i^m \delta y_i^n dxdy,$$

where m and n are powers of the corresponding Taylor basis and h_i is the length scale for the non-dimensionalization of the basis functions to avoid growth of the condition number of the reconstruction matrix with grid refinement [30,39]. For triangular grids, the length scale is defined as

$$h_i = \max(Rad_i, \sqrt{\overline{\Omega}_i})$$

where Rad_i is the radius of the circumcircle of the control volume. The following cubic reconstruction ($k = 3$) polynomial in zero-mean basis form is presented to illustrate the relation among the indexes l, m and n

$$u_i(\mathbf{x}) = \bar{u}_i + \sum_{l=1}^{9} u_i^l \varphi_{l,i}(\mathbf{x}) = \bar{u}_i + u_i^1 \delta x_i + u_i^2 \delta y_i + u_i^3 \left(\delta x_i^2 - \overline{\delta x_i^2}\right) + u_i^4 (\delta x_i \delta y_i - \overline{\delta x_i \delta y_i}) + u_i^5 \left(\delta y_i^2 - \overline{\delta y_i^2}\right)$$

$$+ u_i^6 \left(\delta x_i^3 - \overline{\delta x_i^3}\right) + u_i^7 \left(\delta x_i^2 \delta y_i - \overline{\delta x_i^2 \delta y_i}\right) + u_i^8 \left(\delta x_i \delta y_i^2 - \overline{\delta x_i \delta y_i^2}\right) + u_i^9 \left(\delta y_i^3 - \overline{\delta y_i^3}\right)$$

Because of the use of the zero-mean basis, the reconstruction polynomial $u_i(\mathbf{x})$ is always conservative in the sense

$$\frac{1}{\overline{\Omega}_i} \iint\limits_{\Omega_i} u_i(\mathbf{x})dxdy = \bar{u}_i.$$

In the CLS reconstruction, the constitutive relations to determine the unknowns u_i^l, $l = 1, 2, \cdots, DOF(k)$ are constructed by requiring that the cell averages of the reconstruction polynomial $u_i(\mathbf{x})$ and its various orders of spatial derivatives are conserved on S_i, namely, for all $\Omega_j \in S_i$,

$$\frac{1}{\overline{\Omega}_j} \int\limits_{\Omega_j} \frac{\partial^{m+n} u_i(\mathbf{x})}{\partial x^m \partial y^n} dxdy = \frac{1}{\overline{\Omega}_j} \int\limits_{\Omega_j} \frac{\partial^{m+n} u_j(\mathbf{x})}{\partial x^m \partial y^n} dxdy, \quad 0 \leq m+n \leq M \tag{7}$$

where $M \leq k$. By substituting Eq. (6) into Eq. (7), we obtain the following linear equations

$$\sum_{l=1}^{DOF(k)} u_i^l \left(\frac{1}{\overline{\Omega}_j} \int\limits_{\Omega_j} \frac{\partial^{m+n} \varphi_{l,i}(\mathbf{x})}{\partial x^m \partial y^n} dxdy\right) = \delta_{m+n}^0 (\bar{u}_j - \bar{u}_i) + \sum_{l=1}^{DOF(k)} u_j^l \left(\frac{1}{\overline{\Omega}_j} \int\limits_{\Omega_j} \frac{\partial^{m+n} \varphi_{l,j}(\mathbf{x})}{\partial x^m \partial y^n} dxdy\right) \tag{8}$$

for all $\Omega_j \in S_i$. We define $\mathbf{u}_i = [u_i^1, u_i^2, \ldots, u_i^{DOF(k)}]^T$ and rewrite Eq. (8) in the vector form

$$\mathbf{A}_j^i \mathbf{u}_i = \mathbf{B}_j^i \mathbf{u}_j + \mathbf{b}_j^i \tag{9}$$

where

$$\mathbf{A}_j^i = \left[\frac{1}{\overline{\Omega}_j} \int\limits_{\Omega_j} \frac{\partial^{m+n} \varphi_{l,i}(\mathbf{x})}{\partial x^m \partial y^n} dxdy\right]_{(DOF(M)+1) \times DOF(k)}$$

$$\mathbf{B}_j^i = \left[\frac{1}{\overline{\Omega}_j} \int\limits_{\Omega_j} \frac{\partial^{m+n} \varphi_{l,j}(\mathbf{x})}{\partial x^m \partial y^n} dxdy\right]_{(DOF(M)+1) \times DOF(k)}$$

$$\mathbf{b}_j^i = \left[\delta_{m+n}^0 (\bar{u}_j - \bar{u}_i)\right]_{(DOF(M)+1) \times 1}. \tag{10}$$

Table 1
The number of linear equations and the number of unknowns in different order CLS reconstruction schemes.

Reconstruction	Linear	Quadratic	Cubic
k	1	2	3
Equations	3	9	18
Unknowns	2	5	9

In practice, in Eq. (8), the p ($p = m + n$)-order derivatives are associated with a weight function $w_{i,p}$ to control the relative importance of equations with different p. In the present paper, weight functions $w_{i,p}$, $p = 0, \ldots, M$ are in the form

$$w_{i,p} = (wh_i)^p. \tag{11}$$

The matrices in Eq. (10) are redefined as

$$\mathbf{A}_j^i = \left[\frac{w_{i,m+n}}{\overline{\Omega}_j} \int_{\Omega_j} \frac{\partial^{m+n} \varphi_{l,i}(\mathbf{x})}{\partial x^m \partial y^n} dxdy \right]_{(DOF(M)+1) \times DOF(k)}$$

$$\mathbf{B}_j^i = \left[\frac{w_{i,m+n}}{\overline{\Omega}_j} \int_{\Omega_j} \frac{\partial^{m+n} \varphi_{l,j}(\mathbf{x})}{\partial x^m \partial y^n} dxdy \right]_{(DOF(M)+1) \times DOF(k)}.$$

Remark 1. The weight functions significantly affect the accuracy of the numerical scheme. It is noticed that the weight functions defined in Eq. (11) have only one free parameter which can be optimized through numerical experiments presented in Section 3.1. We recognize that the optimal value of w is related to the specific grids and solutions being reconstructed. In the present paper, we choose regular grids and smooth solutions to calibrate w. This is a reasonable choice since it is always desirable to generate grids as regular as possible and accuracy of the reconstruction can be rigorously quantified only for smooth functions. Because of these limitations, only the sub-optimal value of w can be obtained, which is $0.2 \sim 0.3$ according to the numerical experiments. One can also increase the number of free parameters in the weight functions to further optimize the performance of the reconstruction procedure. This approach is however more difficult to obtained universal optimal parameters. Nevertheless, the free parameters determined through the above procedure are used in all test cases of the present paper and the predicted numerical results are significantly more accurate than the high order k-exact FV schemes especially for smooth solutions without shock waves.

The following linear equation system is obtained by collecting Eq. (9) corresponding to the three face-neighbors with j being $j1$, $j2$ and $j3$,

$$\begin{pmatrix} \mathbf{A}_{j1}^i \\ \mathbf{A}_{j2}^i \\ \mathbf{A}_{j3}^i \end{pmatrix} \mathbf{u}_i = \begin{pmatrix} \mathbf{B}_{j1}^i \\ \mathbf{0} \\ \mathbf{0} \end{pmatrix} \mathbf{u}_{j1} + \begin{pmatrix} \mathbf{0} \\ \mathbf{B}_{j2}^i \\ \mathbf{0} \end{pmatrix} \mathbf{u}_{j2} + \begin{pmatrix} \mathbf{0} \\ \mathbf{0} \\ \mathbf{B}_{j3}^i \end{pmatrix} \mathbf{u}_{j3} + \begin{pmatrix} \mathbf{b}_{j1}^i \\ \mathbf{b}_{j2}^i \\ \mathbf{b}_{j3}^i \end{pmatrix} \tag{12}$$

which can be rewritten in a compact form as

$$\mathbf{A}_i \mathbf{u}_i = \sum_{j \in S_i} \mathbf{B}_j \mathbf{u}_j + \mathbf{b}_i \tag{13}$$

Generally, in two-dimensional cases, we choose $M = k - 1$. Therefore, the number of linear equations in Eq. (13) is $3 * [DOF(k-1) + 1]$ and always larger than $DOF(k)$, making the system over-determined. The number of linear equations and the number of unknowns for different order CLS reconstruction schemes are listed in Table 1.

The over-determined linear equation system described by Eq. (13) is solved using the method of least-squares. The corresponding normal equations are

$$\mathbf{A}_i^T \mathbf{A}_i \mathbf{u}_i - \sum_{j \in S_i} \mathbf{A}_i^T \mathbf{B}_j \mathbf{u}_j = \mathbf{A}_i^T \mathbf{b}_i \tag{14}$$

In one-dimensional cases, Eq. (14) represents a block-tridiagonal linear equation system that can be solved directly. It has been shown in [1] that this approach is stable under CFL conditions. While in two-dimensional cases, as the indexes of the central cell and its face-neighbors are usually not adjacent, Eq. (14) represents a large sparse linear equation system for which both direct and iterative solvers are computationally very expensive. Therefore, it is of crucial importance to design an efficient solution procedure. In this paper, it will be shown that the present scheme can be very efficient if an iterative solver for the CLS reconstruction is coupled properly with the time integration procedure. The detailed solution procedure will be discussed in Section 2.3. Here only the iterative solution procedure for solving Eq. (14) is introduced.

In this paper, the Gauss–Seidel method is used to solve Eq. (14). In practice, we solve Eq. (13) using the method of least-squares based on the singular value decomposition (SVD), i.e.
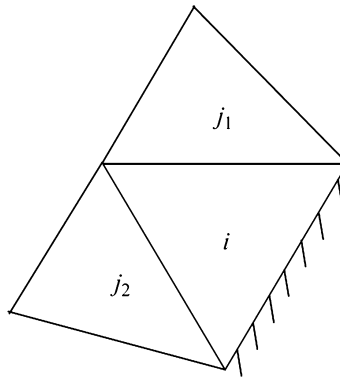
Fig. 2. Reconstruction stencil for a boundary cell i.

$$\mathbf{u}_i^{(s)} = \mathbf{A}_i^{\dagger} \left(\sum_{j \in S_i, \, j < i} \mathbf{B}_j \mathbf{u}_j^{(s)} + \sum_{j \in S_i, \, j > i} \mathbf{B}_j \mathbf{u}_j^{(s-1)} + \mathbf{b}_i \right) \tag{15}$$

where $\mathbf{A}_i^{\dagger}$ is the general inverse of the matrix $\mathbf{A}_i$ and s denotes the iteration step. In practical implementation, $\mathbf{A}_i^{\dagger}$ is stored to improve the computational efficiency. According to Table 1, the CLS reconstruction has a memory overhead closed to the k-exact reconstruction [40].

Remark 2. One concern of the polynomial reconstruction is the large condition number encountered when high order polynomial is reconstructed. Numerical study of Section 3.1 shows that the condition number of the iteration procedure (15) can be well controlled. It is also observed that a larger w in the weight function defined in Eq. (11) will result in a smaller condition number. Therefore, in practical implementations, the parameter w can be chosen slightly larger than the optimal value obtained through numerical experiments to make the scheme being both accurate and robust. It is noticed that the condition number considered here is only associated with the iteration procedure of Eq. (15). The condition number of the large sparse system of equations corresponding to the CLS reconstruction is difficult to analyze. However, no difficulty in convergence is experienced in the applications of the present schemes.

Boundary treatment is necessary for the CLS reconstruction because for a boundary cell, as shown in Fig. 2, the number of face-neighboring cells is less than the number of faces, i.e., $S_i = \{\Omega_{j_1}, \Omega_{j_2}\}$, which results in a decrease of the number of linear equations.

According to Gustafsson [41], the overall accuracy of the numerical solution can be kept at the designed high order if the approximation at the boundary has one-order lower accuracy than at inner points. Therefore, the boundary treatment in the present paper is to use a reconstruction scheme at boundary cells one-order lower in accuracy than the reconstruction scheme at inner cells. The reconstruction scheme at boundary cells is

$$\begin{pmatrix} \mathbf{A}_{j1}^i \\ \mathbf{A}_{j2}^i \end{pmatrix} \mathbf{u}_i = \begin{pmatrix} \mathbf{B}_{j1}^i \\ \mathbf{0} \end{pmatrix} \mathbf{u}_{j1} + \begin{pmatrix} \mathbf{B}_{j2}^i \\ \mathbf{0} \end{pmatrix} \mathbf{u}_{j2} + \begin{pmatrix} \mathbf{b}_{j1}^i \\ \mathbf{b}_{j2}^i \end{pmatrix} \tag{16}$$

where

$$\mathbf{u}_i = \left(u_i^l \right)_{DOF(k-1) \times 1},$$

$$\mathbf{A}_j^i = \left(\frac{w_{i,m+n}}{\overline{\Omega}_j} \int_{\Omega_j} \frac{\partial^{m+n} \varphi_{l,i}(\mathbf{x})}{\partial x^m \partial y^n} dx dy \right)_{(DOF(k-1)+1) \times DOF(k-1)}$$

$$\mathbf{B}_j^i = \left(\frac{w_{i,m+n}}{\overline{\Omega}_j} \int_{\Omega_j} \frac{\partial^{m+n} \varphi_{l,j}(\mathbf{x})}{\partial x^m \partial y^n} dx dy \right)_{(DOF(k-1)+1) \times DOF(k)}$$

$$\mathbf{b}_j^i = \left(\delta_{m+n}^0 (\bar{u}_j - \bar{u}_i) \right)_{(DOF(k-1)+1) \times 1}.$$

Since straight segments approximation for curved boundary would degrade the accuracy and stall the convergence of the high order methods, the method of [42] is used to treat the curved boundary. For the third and fourth order CLSFV method, the curved line 2–3 in Fig. 3 is approximated by an arc of the circle passing through vertices 2 and 3. The radius of the circle is taken to be the average of the radii of the circle passing through vertices $2'$, 2 and 3 and the circle passing through vertices 2, 3 and $3'$. Two additional control points for the curved line, namely vertices 4 and 5 shown in Fig. 4, are obtained from the arc.
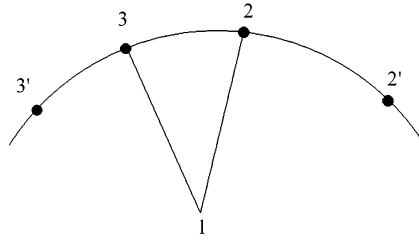
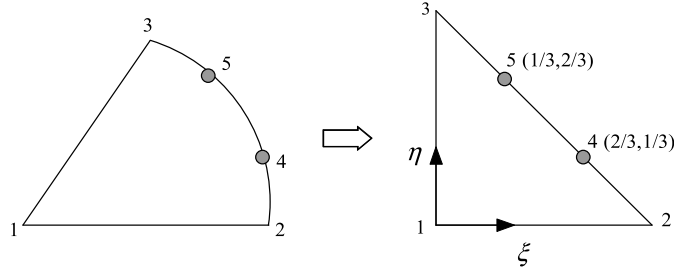**Fig. 3.** Representation for the curved line.

Fig. 4. The isoparametric transformation for the curved triangle.

The curved boundary treatment brings difficulty of face and volume integrals on curved elements. The method to perform the integrals is to transform the curved triangle to regular triangle using the isoparametric transformation. The isoparametric transformation for the curved line in Fig. 4 can be written as

$$\mathbf{x}(\xi) = \sum_{k=2}^{5} v_k(\xi)\mathbf{x}_k,$$

$$v_2(\xi, \eta) = -4.5(\xi - 1)(\xi^2 - \xi + 2/9),$$

$$v_3(\xi, \eta) = 13.5\xi(\xi^2 - 5\xi/3 + 2/3),$$

$$v_4(\xi, \eta) = -13.5\xi(\xi^2 - 4\xi/3 + 1/3),$$

$$v_5(\xi, \eta) = 4.5\xi(\xi^2 - \xi + 2/9).$$

The flux integral on the curved boundary can be computed using the following Gauss quadrature formula

$$\int_{\widehat{23}} \mathbf{f} \bullet \mathbf{n} \, dl \approx \sum_{\varphi=1}^{NG} \omega_\varphi \mathbf{f}\big(\mathbf{U}\big(\mathbf{x}(\xi_\varphi)\big)\big) \bullet \left(\frac{dy}{d\xi}, -\frac{dx}{d\xi}\right)\bigg|_{\xi=\xi_\varphi}.$$

The isoparametric transformation for triangle shown in Fig. 4 can be written as

$$\mathbf{x}(\xi, \eta) = \sum_{k=1}^{5} v_k(\xi, \eta)\mathbf{x}_k,$$

$$v_1(\xi, \eta) = 1 - \xi - \eta,$$

$$v_2(\xi, \eta) = \xi(1 - 3\eta)(1 - 1.5\eta),$$

$$v_3(\xi, \eta) = \eta(1 - 4.5\xi\eta),$$

$$v_4(\xi, \eta) = 9\xi\eta(1 - 1.5\eta),$$

$$v_5(\xi, \eta) = 4.5\xi\eta(-1 + 3\eta).$$

For an arbitrary function $f(\mathbf{x})$, the volume integral would be

$$\int_{\Omega} f(\mathbf{x})dxdy = \int_{\Omega^{iso}} f\big(\mathbf{x}(\xi, \eta)\big)\frac{\partial(x, y)}{\partial(\xi, \eta)}d\xi d\eta.$$

To suppress non-physical oscillations near discontinuities, the WBAP limiter [40,43] based on the secondary reconstruction [44] is used in supersonic and transonic flow simulations. The WBAP-L2 limiter

$$W = W^{L2}(1, \theta_1, \cdots, \theta_J) = \frac{n_P + \sum_{k=1}^{J} 1/\theta_k^{p-1}}{n_P + \sum_{k=1}^{J} 1/\theta_k^{p}}$$

is used and the parameters are taken as $p = 4$, and $n_P = 10$. The successive limiting procedure in terms of characteristic variables is used.

Furthermore, a problem-independent shock detector [44] is introduced to improve the efficiency of the limiting procedure. The shock detector presented is used solely for improving the computational efficiency as the WBAP limiter is accuracy-preserving for smooth numerical solutions [40]. The shock detector relies on the smoothness indicator IS_i defined by

$$IS_i = \frac{\sum_j |u_i(\mathbf{x}_i) - u_j(\mathbf{x}_i)|}{N_j h_i^{(k+1)/2} \max(\bar{u}_j, \bar{u}_i)}, \quad j \in S_i,$$

where N_j stands for the number of face-neighboring cells and $N_j = 3$ for triangular cell. The following condition is used to distinguish the smooth region from the region near discontinuities

$$u_i(\mathbf{x}_i) - u_j(\mathbf{x}_i) = \begin{cases} O(h_i^{k+1}), & \text{in smooth region,} \\ O(1), & \text{near discontinuity.} \end{cases}$$

Therefore, as the cell size $h_i \to 0$, $IS_i \to 0$ in smooth regions and $IS_i \to \infty$ near the discontinuities. The shock detector is defined by

$$(IS_i < \bar{S}_{dis}) = \begin{cases} \text{true,} & \text{smooth region,} \\ \text{false,} & \text{shock region.} \end{cases}$$

Generally, $\bar{S}_{dis} = 1$ is chosen for the second-order and third-order schemes and $\bar{S}_{dis} = 3$ for the fourth-order scheme. These parameters work well for all test cases of the present paper and are problem-independent.

2.3. CLS reconstruction and implicit dual time stepping technique coupled solution procedure

The CLS reconstruction is implicit since it is required to solve a large sparse system of linear equations when performing the reconstruction. If the converged solution of the sparse linear equation system is computed every single time step, both direct and iterative solvers are computationally very expensive. Therefore, this method is not suitable to use in conjunction with explicit time integration schemes for computing the unsteady flows. Fortunately, in some important cases, the iterative solver of the CLS reconstruction can be coupled with the time integration scheme to achieve high computational efficiency. The first case is the steady-state simulation in terms of the time-dependent equations in which the temporal accuracy will not affect the converged steady-state solutions. Therefore, Eq. (15), the iterative solver of the CLS reconstruction, need not reach full convergence, and can be implemented only once in a single time step. The coupling between the CLS reconstruction and the temporal discretization scheme makes the two procedures achieve their convergence synchronously. The second case is the unsteady simulation using the dual time stepping technique [45,46] which can be considered as solving a modified steady problem by advancing in pseudo time at each physical time step. Similar to the steady-state simulation, the iteration in the CLS reconstruction can be also performed only once in every pseudo time step. Since the steady-state simulation can be considered as a special case of unsteady simulation using the dual time stepping technique by simply neglecting the physical time derivative terms, only the unsteady case will be discussed in detail.

For unsteady flow simulations, not only the high order spatial discretization but also the high-order temporal discretization is necessary to obtain high order accurate numerical solution. The high order implicit time integration scheme used in this paper is the three-stage, fourth-order accurate singly-diagonally implicit Runge–Kutta (SDIRK) method [47]. By using this method, Eq. (4) is integrated in time as

$$\frac{\bar{\mathbf{U}}^{n+1} - \bar{\mathbf{U}}^n}{\Delta t} = \sum_{\alpha=1}^{3} \boldsymbol{\beta}_\alpha \mathbf{R}(\mathbf{U}^\alpha) \tag{17}$$

where

$$\frac{\bar{\mathbf{U}}^\alpha - \bar{\mathbf{U}}^n}{\Delta t} = \sum_{\beta=1}^{\alpha} \boldsymbol{\alpha}_{\alpha\beta} \mathbf{R}(\mathbf{U}^\beta). \tag{18}$$

The specific values of $\boldsymbol{\beta}_\alpha$ and $\boldsymbol{\alpha}_{\alpha\beta}$ are listed in Table 2.

Eq. (18) is implicit, and for the Euler equations, is nonlinear. The dual time stepping technique is used to solve this nonlinear system of equations, in which a pseudo-time variable τ is introduced. The time integration scheme for one pseudo-time step is

$$\left(\frac{\mathbf{I}}{\Delta \tau} + \frac{\mathbf{I}}{\Delta t} - \boldsymbol{\alpha}_{\alpha\alpha} \frac{\partial \mathbf{R}}{\partial \bar{\mathbf{U}}} \right) \Delta \bar{\mathbf{U}} = \mathbf{R}_t \tag{19}$$

Table 2
Butcher tableau for the three-stage, fourth-order SDIRK method. $\zeta = 0.128886400515$.

ζ	0	0	ζ
$1/2 - \zeta$	ζ	0	$1/2$
2ζ	$1 - 4\zeta$	ζ	$1 - \zeta$
$1/6/(2\zeta - 1)^2$	$(4\zeta^2 - 4\zeta + 2/3)/(2\zeta - 1)^2$	$1/6/(2\zeta - 1)^2$	

where

$$\Delta\bar{\mathbf{U}} = \bar{\mathbf{U}}^{(s+1)} - \bar{\mathbf{U}}^{(s)},$$

$$\mathbf{R}_t = \frac{1}{\Delta t}\left(\bar{\mathbf{U}}^n - \bar{\mathbf{U}}^{(s)}\right) + \boldsymbol{\alpha}_{\alpha\alpha}\mathbf{R}\left(\mathbf{U}^{(s)}\right) + \sum_{\beta=1}^{\alpha-1}\boldsymbol{\alpha}_{\alpha\beta}\mathbf{R}\left(\mathbf{U}^{\beta}\right).$$

The solution is advanced using local pseudo-time steps $\Delta\tau$ until $\bar{\mathbf{U}}^{(s+1)}$ converges to $\bar{\mathbf{U}}^\alpha$. Eq. (19) is solved by the matrix-free LU-SGS approach [48]. In solving Eq. (19), the iterative solver (15) is solved once in a pseudo-time step. The CLS reconstruction and implicit dual time stepping technique coupled solution procedure is described below for the advancement in one physical time step.

Algorithm. Unsteady flow solver using the implicit reconstruction and implicit time integration coupled iteration method.

$\bar{\mathbf{U}}^0 = \bar{\mathbf{U}}^n$	initialization
Do $\alpha = 1, 3$	the α-th stage of the SDIRK
$\bar{\mathbf{U}}^{(1)} = \bar{\mathbf{U}}^{\alpha-1}$	initialization for the inner iteration
Do $s = 1$, max_inner_iteration_step	inner iteration in terms of the pseudo-time step at the α-th stage
Do $i = 1, N$	perform the reconstruction iteration cell by cell
$\mathbf{u}_i^{(s)} = \mathbf{A}_i^\dagger(\sum_{j\in S_i, j<i}\mathbf{B}_j\mathbf{u}_j^{(s)} + \sum_{j\in S_i, j>i}\mathbf{B}_j\mathbf{u}_j^{(s-1)} + \mathbf{b}_i)$	Gauss–Seidel iteration step
End Do	
Compute $\mathbf{R} = \mathbf{R}(\mathbf{U}^s)$	numerical fluxes evaluation
Solve $(\frac{\mathbf{I}}{\Delta\tau} + \frac{\mathbf{I}}{\Delta t} - \boldsymbol{\alpha}_{\alpha\alpha}\frac{\partial\mathbf{R}}{\partial\bar{\mathbf{U}}})\Delta\bar{\mathbf{U}} = \mathbf{R}_t$	implicit dual time stepping time integration
$\bar{\mathbf{U}}^{(s+1)} = \bar{\mathbf{U}}^{(s)} + \Delta\bar{\mathbf{U}}$	update the cell-averages
$residual(\text{s}) = L_1(\Delta\rho)$	compute the L_1 residual in terms of density
If $residual(\text{s})/residual(1) < \varepsilon$ exit	convergence check
End Do	
$\bar{\mathbf{U}}^\alpha = \bar{\mathbf{U}}^{(s+1)}$	the converged solution of the inner iterations
End Do	
$\bar{\mathbf{U}}^{n+1} = \bar{\mathbf{U}}^n + \Delta t\sum_{\alpha=1}^3\boldsymbol{\beta}_\alpha\mathbf{R}(\mathbf{U}^\alpha)$	the solution for next physical time step

From the above algorithm, we can see that the coupling of the CLS reconstruction with the dual time stepping implicit Runge–Kutta method is in fact very close to performing the traditional reconstruction, such as the *k*-exact reconstruction in a dual time stepping implicit scheme, as the iteration in the CLS reconstruction is carried out only once in a cell by cell manner. Therefore, by using the coupled iteration method, the implicit property of the CLS reconstruction does not lead to extra computational cost, which will significantly improve the efficiency of the CLSFV method.

For steady-state simulations, since the temporal accuracy is not important, the above solution procedure can be simplified by replacing Eqs. (17) and (19) respectively with

$$\bar{\mathbf{U}}^{n+1} = \bar{\mathbf{U}}^n + \Delta\bar{\mathbf{U}} \tag{20}$$

and

$$\left(\frac{\mathbf{I}}{\Delta\tau} - \frac{\partial\mathbf{R}}{\partial\bar{\mathbf{U}}}\right)\Delta\bar{\mathbf{U}} = \mathbf{R} \tag{21}$$

and setting $\Delta t = \infty$, $s = 1$ and $\alpha = 1$. It is observed in the numerical test that the convergence speed for steady-state flow problems will be accelerated if the matrix-free, LU-SGS preconditioned GMRES approach [48] is used to solve the linear system in Eq. (21).

To study the convergence property of the CLS reconstruction and implicit dual time stepping technique coupled solution procedure, the convergence histories of the fourth order CLSFV scheme in terms of both the numerical solution and the CLS reconstruction in the simulation of steady flow past the NACA0012 airfoil are shown in Fig. 5. The results indicate that the two procedures achieve their convergence almost synchronously. Fig. 5 also compares the convergence histories of the
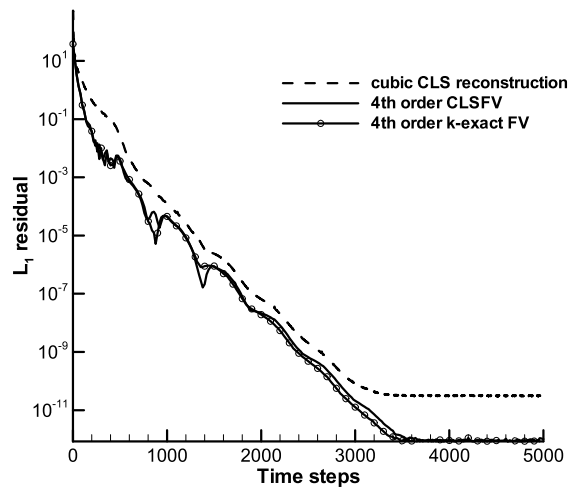
Fig. 5. Convergence history comparison among the cubic CLS reconstruction and the fourth order CLSFV and *k*-exact FV schemes for subsonic flow past a NACA0012 airfoil problem.
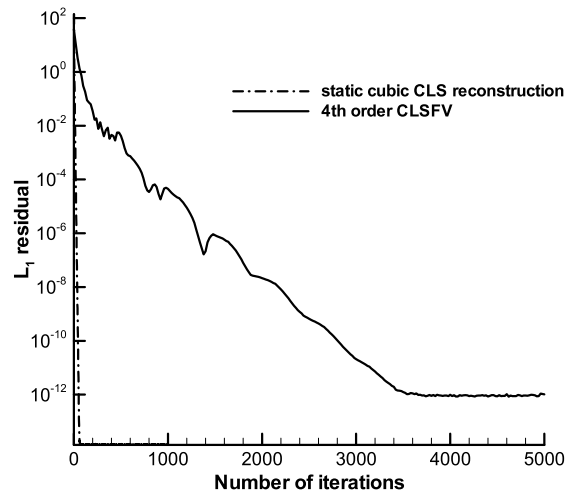

Fig. 6. Convergence history comparison among the static cubic CLS reconstruction and the fourth order CLSFV scheme for subsonic flow past a NACA0012 airfoil problem.

present CLSFV scheme and the fourth order *k*-exact FV scheme. The convergence speeds of the two schemes in terms of time steps are almost the same, which demonstrates that the coupled solution procedure is as efficient as the traditional implicit FV scheme and the implicit CLS reconstruction does not adversely affect the efficiency of the CLSFV scheme. To further explain this fact, the convergence history of the static CLS reconstruction in one time step is compared with the history of convergence of the fourth order *k*-exact FV scheme in solving the steady flow past the NACA0012 airfoil in Fig. 6. It can be seen from Fig. 6 that the convergence speed of the static CLS reconstruction is hundreds times faster than the time integration scheme, which means that the convergence speed of the CLSFV scheme is mainly depended on the time integration method.

For unsteady flow simulation, the dual time stepping technique solve a modified steady flow in every pseudo time. Therefore, the discussions presented above can be also applied to the unsteady flow simulation. The feasibility of the present method for computing specific unsteady flows depends mainly on if the implicit schemes are suitable for simulating such flows. In fact, it has been found that in some important cases, computing the unsteady flow using the implicit time stepping schemes is beneficial. For example, Zhong [49] developed the implicit scheme to treat the stiff source terms in high-speed nonequilibrium reactive flow simulation. Martín et al. [50] used the implicit scheme to improve computational efficiency of direct numerical simulation (DNS) of wall-bounded compressible turbulence.
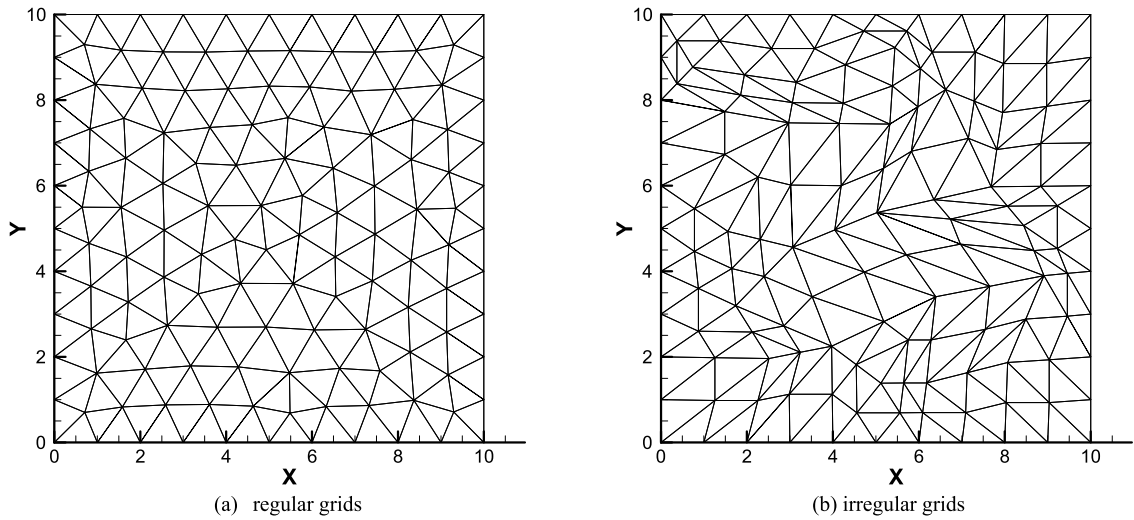
(a) regular grids   (b) irregular grids

Fig. 7. Regular and irregular grids with size $h = 1$ for the isentropic vortex problem.

3. Numerical results

The third and fourth order CLSFV schemes are applied to solve a number of two-dimensional benchmark test cases to assess the schemes' accuracy, efficiency and shock capturing capability.

3.1. Isentropic vortex problem

The isentropic vortex transport problem [51] is used to test the accuracy of the high order CLSFV schemes. The mean flow is $(\rho, u, v, p) = (1, 1, 1, 1)$. An isentropic vortex is added to the mean flow with the following perturbations

$$(\delta u, \delta v) = \frac{\chi}{2\pi} e^{0.5(1-r^2)} (-\bar{y}, \bar{x}),$$

$$\delta T = -\frac{(\gamma - 1)}{\chi^2} 8\gamma \pi^2 e^{1-r^2},$$

$$\delta \big(S = p/\rho^r \big) = 0,$$

where $(\bar{x}, \bar{y}) = (x - 5, y - 5)$, $r^2 = \bar{x}^2 + \bar{y}^2$, and the vortex strength $\chi = 5$. Translational periodic boundary conditions are imposed for the left/right and top/bottom boundaries respectively. The computations are performed until $t = 2.0$. The two types of grids used in the computation, namely the regular and irregular grids, are shown in Fig. 7.

The grid sizes are chosen to be 1 to 1/16, and the corresponding physical time steps are 2/5 to 2/80. The CFL number for the local pseudo time step is 40 and the convergence criterion for the inner iteration is $\varepsilon = 10^{-5}$. The accuracy tests of the second, third and fourth order k-exact FV schemes are also performed to compare with the high order CLSFV schemes.

Before presenting the detailed numerical results, the determination of the parameter w in weight functions defined in Eq. (11) is firstly discussed. The method used here is to study the relation between parameter w and the computational efficiency defined by

$$\eta = \frac{1}{t_{cpu} \cdot \Delta}$$

where t_{cpu} is the CPU time and Δ is the error of the numerical solution. It is further defined that η_1 is the efficiency in terms of the L_1 error and η_∞ is the efficiency in terms of the L_∞ error. Fig. 8 shows the computational efficiency of the third and fourth order CLSFV schemes on $h = 1/4$ regular mesh with different w. The results in Fig. 8 show that the third order CLSFV scheme with smaller w has higher efficiency and the fourth order CLSFV scheme achieves the highest efficiency at w around 0.2.

The parameter w also affects the condition number of the iteration procedure (15) of the CLS reconstruction. The maximal condition numbers on the regular and irregular grids are shown in Figs. 9 and 10. The results in these two figures show that the condition number does not grow noticeably when the grid gets finer, which demonstrates the effect of the scaling technique [30] applied to the basis functions. It also observed that a larger w will produce smaller condition number in the iteration procedure. To design accurate and robust numerical schemes, the parameter w can be chosen slightly larger than the optimal value obtained due to efficiency consideration. In practice, $w = 0.2$ is selected for the third order CLSFV scheme and $w = 0.3$ is selected for the fourth order CLSFV scheme. We would like to point out that the optimal weight function
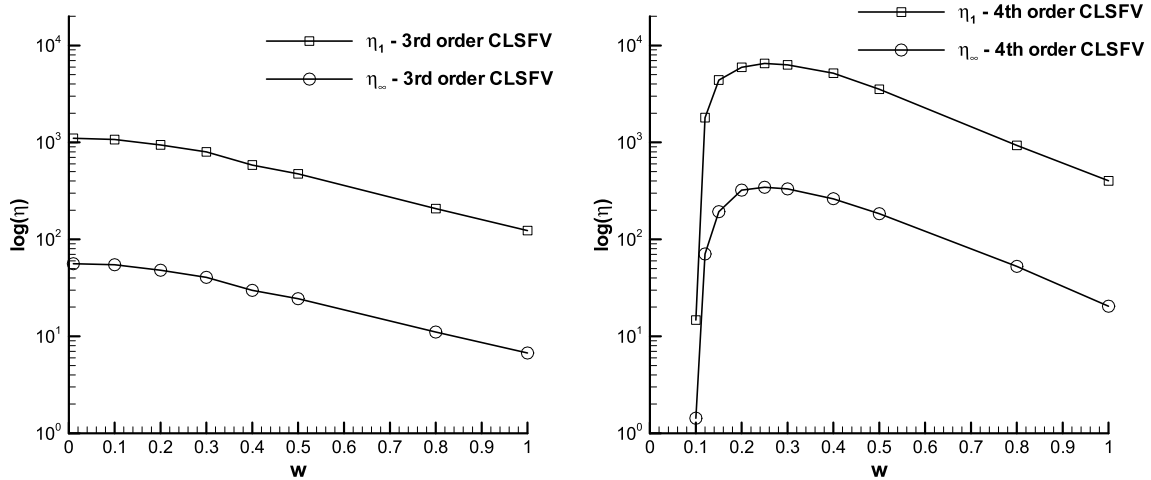
Fig. 8. Computational efficiency on $h = 1/4$ regular mesh with different w.
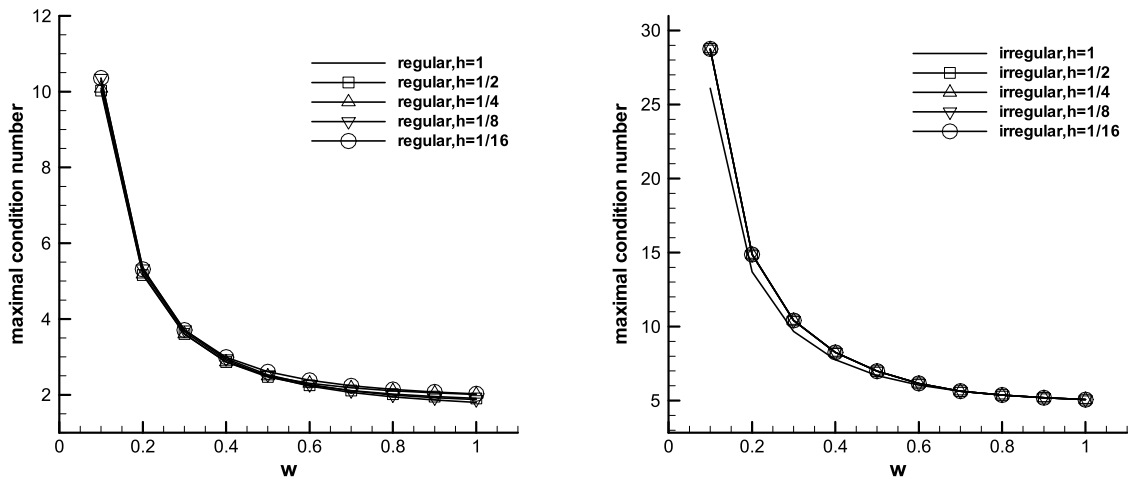

Fig. 9. Maximal condition numbers for third order CLSFV scheme with different w.

depends only on the geometry of the grid. In practical applications, the grid should be as regular as possible, which means that we need to calibrate the optimal weight only once on regular grid by solving a simple test case, and then use this optimal weight for all other test cases. Therefore, the free parameter in the weight function does not pose any real problem in the application of the schemes.

The errors of density in terms of L_1 and L_∞ norms and the rates of convergence on regular grids are listed in Table 3. The accuracy comparison is shown in Fig. 11 and the efficiency comparison is shown in Fig. 12. The results in Table 3 and Fig. 11 show that all the schemes achieve the theoretical high order accuracy and the solutions computed by the CLSFV schemes are much more accurate than those computed by the k-exact FV schemes of the same order of accuracy. The results in Fig. 12 show that the CLSFV schemes can achieve the same accuracy using less CPU time, which means that the CLSFV schemes are more efficient than the k-exact FV schemes of the same level of accuracy. Furthermore, the high order schemes are more efficient than the second order scheme at the high accuracy level on sufficiently fine grids. For example, on $h = 1/16$ grid, the fourth order CLSFV scheme is at least two orders of magnitude more efficient than the second order FV scheme.

In Fig. 13, the effect of the parameter w in the weight function is studied by comparing the numerical results obtained by using $w = 1$ (parameter free version of the proposed scheme) and the optimal parameter $w = 0.3$ in the fourth order CLSFV scheme. The results show that in both cases the schemes achieve fourth order accuracy, but the scheme with optimal parameter generates much smaller error when spending the same CPU time. Therefore, the CLSFV scheme using the optimal weight is much more efficient than the parameter free version of the proposed scheme. The introduction of the optimal weight can be considered as the optimization procedure of the proposed scheme. Indeed, in the one-dimensional case of the present scheme, we have shown that the adoption of the optimal weight can improve the dispersion property of the scheme and lead to higher resolution in the numerical simulation [1].
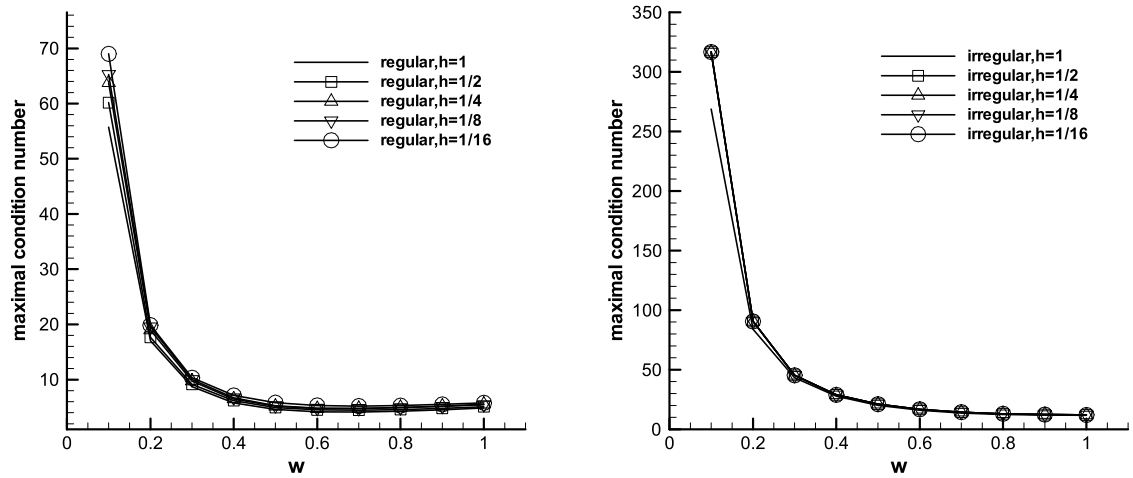
Fig. 10. Maximal condition numbers for fourth order CLSFV scheme with different w.

Table 3
Accuracy test results for the isentropic vortex problem on regular grids.

Schemes	Grid size	L_1 error	Order	L_∞ error	Order
2nd order CLS/k-exact FV	1	8.94E−03		7.31E−02	
	1/2	1.79E−03	2.32	2.84E−02	1.37
	1/4	4.66E−04	1.94	8.94E−03	1.67
	1/8	9.20E−05	2.34	2.34E−03	1.94
	1/16	2.27E−05	2.02	7.21E−04	1.70
3rd order CLS FV	1	5.74E−03		7.52E−02	
	1/2	1.01E−03	2.51	1.85E−02	2.02
	1/4	1.55E−04	2.70	3.05E−03	2.61
	1/8	1.96E−05	2.98	4.25E−04	2.84
	1/16	2.38E−06	3.04	6.04E−05	2.82
3rd order k-exact FV	1	8.80E−03		1.36E−01	
	1/2	1.90E−03	2.21	3.47E−02	1.97
	1/4	3.25E−04	2.54	6.22E−03	2.48
	1/8	4.35E−05	2.90	8.69E−04	2.84
	1/16	5.41E−06	3.01	1.16E−04	2.90
4th order CLS FV	1	3.31E−03		3.31E−02	
	1/2	2.53E−04	3.71	5.74E−03	2.53
	1/4	1.36E−05	4.22	2.57E−04	4.48
	1/8	5.50E−07	4.63	1.61E−05	4.00
	1/16	3.32E−08	4.05	8.04E−07	4.32
4th order k-exact FV	1	4.05E−03		5.14E−02	
	1/2	6.20E−04	2.71	1.27E−02	2.02
	1/4	3.81E−05	4.02	6.43E−04	4.30
	1/8	1.94E−06	4.30	3.69E−05	4.12
	1/16	1.16E−07	4.06	2.27E−06	4.02

The effect of the grid quality is also studied. The errors of density in terms of L_1 and L_∞ norms and the rates of convergence on irregular grids are listed in Table 4. The accuracy comparison is shown in Fig. 14 and the efficiency comparison is shown in Fig. 15. The results in Table 4 and Fig. 14 show that all the high order schemes achieve the theoretical high order accuracy and the solutions computed by the CLSFV schemes are much more accurate than that by the k-exact FV schemes of the same order of accuracy. The results in Fig. 15 show that the CLSFV schemes can achieve the same accuracy using less CPU time, which means that the CLSFV schemes are also more efficient than the k-exact FV schemes of the same order of accuracy on irregular grids. Furthermore, the high order schemes are more efficient than the second order scheme at higher accuracy level.

The CPU time and error comparison of the fourth order CLSFV and k-exact FV schemes using both explicit and implicit Runge–Kutta methods is given in Table 5. The CFL number for the explicit TVD Runge–Kutta method [52] is 1.0. The iteration of the reconstruction in the CLSFV scheme using explicit time integration is performed 10 times in each Runge–Kutta stage. The CLSFV scheme spends three times more CPU time than the k-exact FV scheme using explicit Runge–Kutta method, which indicates that the CLSFV scheme is not optimal in efficiency when used with the explicit time stepping schemes.
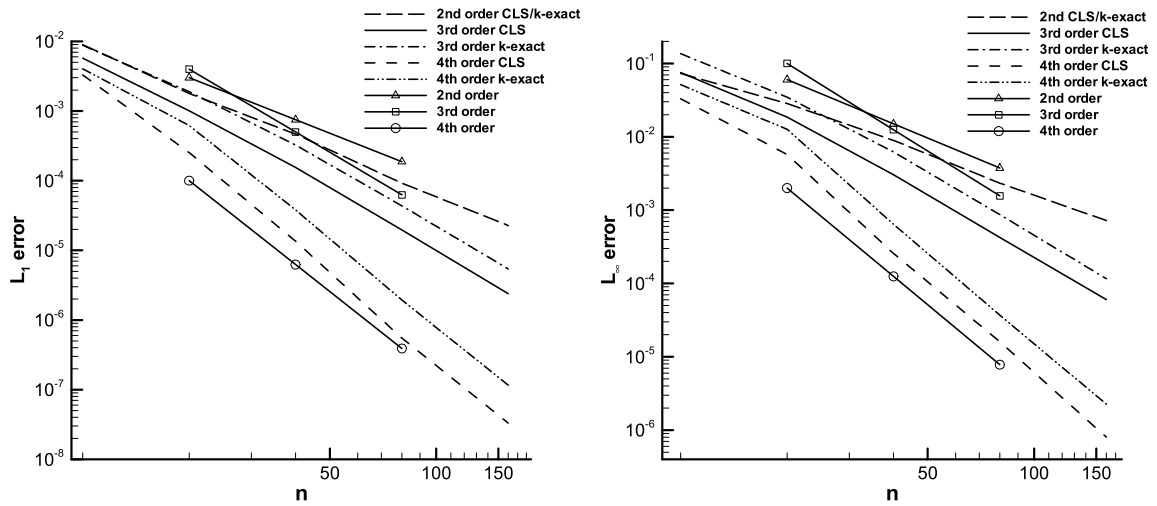
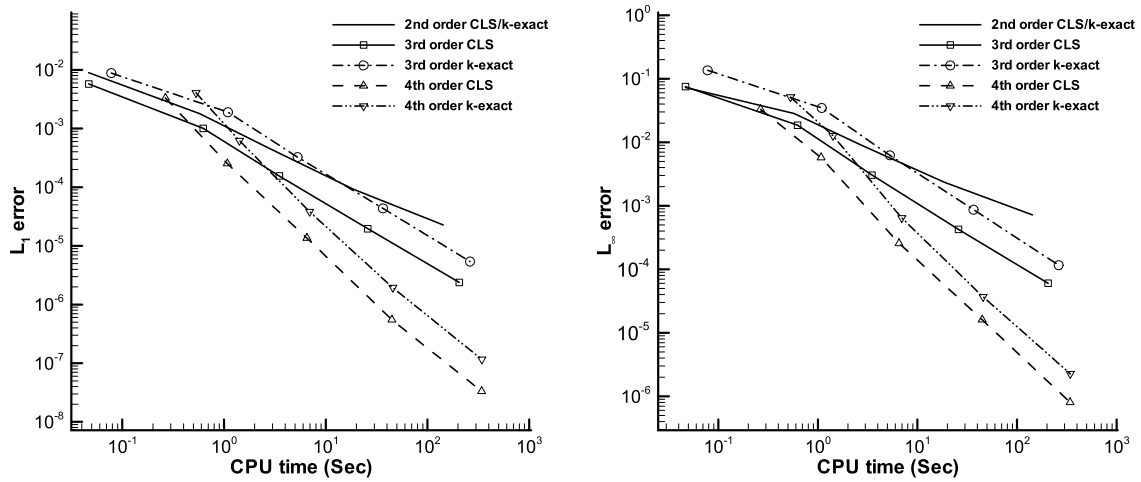**Fig. 11.** Accuracy comparison for the isentropic vortex problem on regular grids.

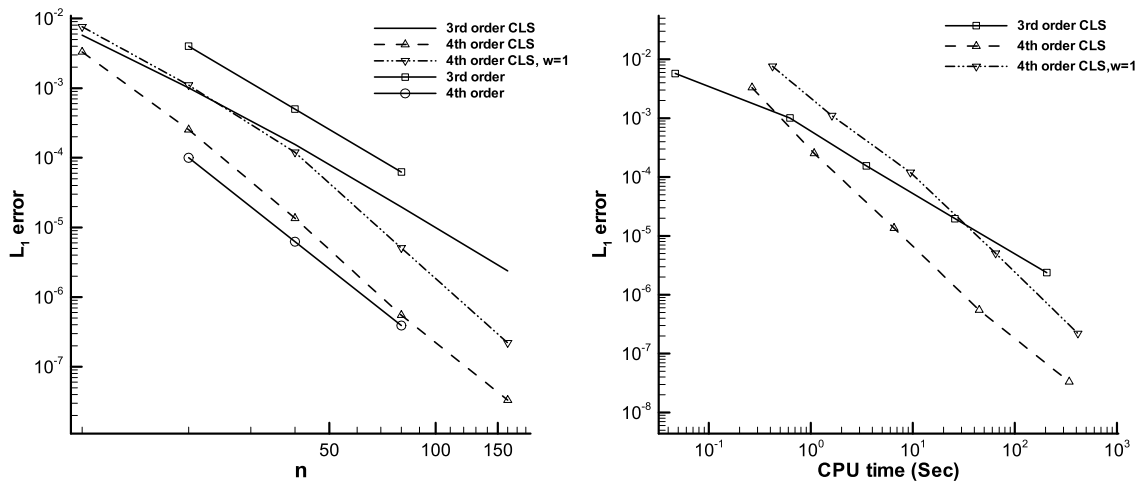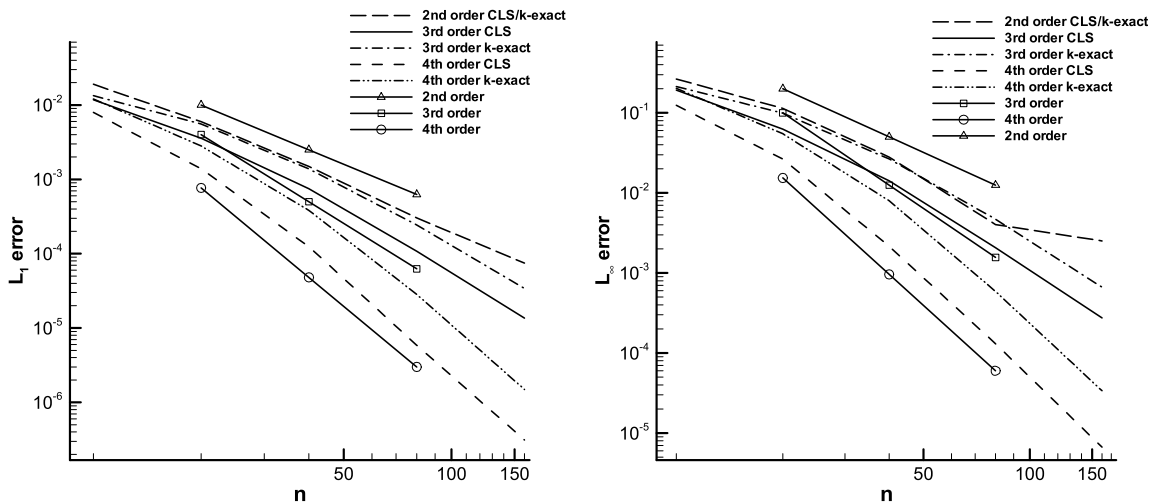**Fig. 12.** Efficiency comparison for the isentropic vortex problem on regular grids.

Fig. 13. Accuracy and efficiency comparison of the two fourth order CLSFV schemes with different values of free parameter on regular grids.

Table 4
Accuracy test results for the isentropic vortex problem on irregular grids.

Schemes	Grid size	L_1 error	Order	L_∞ error	Order
2nd order CLS/k-exact FV	1	1.90E−02		2.65E−01	
	1/2	5.97E−03	1.67	1.14E−01	1.22
	1/4	1.49E−03	2.00	2.80E−02	2.02
	1/8	3.03E−04	2.30	4.02E−03	2.80
	1/16	7.46E−05	2.02	2.52E−03	0.68
3rd order CLS FV	1	1.18E−02		1.92E−01	
	1/2	3.56E−03	1.72	6.27E−02	1.61
	1/4	7.46E−04	2.26	1.42E−02	2.15
	1/8	1.08E−04	2.79	2.06E−03	2.78
	1/16	1.36E−05	2.99	2.75E−04	2.91
3rd order k-exact FV	1	1.34E−02		2.13E−01	
	1/2	5.56E−03	1.26	9.91E−02	1.10
	1/4	1.38E−03	2.01	2.65E−02	1.90
	1/8	2.44E−04	2.50	4.69E−03	2.50
	1/16	3.41E−05	2.84	6.65E−04	2.82
4th order CLS FV	1	7.94E−03		1.24E−01	
	1/2	1.39E−03	2.51	2.65E−02	2.23
	1/4	1.24E−04	3.49	2.15E−03	3.62
	1/8	5.87E−06	4.40	1.30E−04	4.04
	1/16	3.12E−07	4.23	6.69E−06	4.29
4th order k-exact FV	1	1.21E−02		2.02E−01	
	1/2	2.81E−03	2.10	5.48E−02	1.88
	1/4	3.83E−04	2.88	7.96E−03	2.78
	1/8	2.83E−05	3.76	5.88E−04	3.76
	1/16	1.50E−06	4.24	3.38E−05	4.12

Fig. 14. Accuracy comparison for the isentropic vortex problem on irregular grids.

However, as shown in Fig. 12 and Fig. 15, the CLSFV scheme is much more efficient than the k-exact FV scheme in the framework of reconstruction and implicit time integration coupled solution procedure.

3.2. Subsonic flow past a circular cylinder

This case is to calculate the subsonic flows past a circular cylinder at a Mach number of $Ma_\infty = 0.38$. It is chosen to validate the accuracy of the CLSFV schemes in solving problems with curved boundaries. The grids shown in Fig. 16 are the five successively refined O-type grids used in the computation constructed using the method in [53]. The grids consist of 16×9, 32×17, 64×33, 128×65 and 256×129 grid points. The first number refers to the number of points in the circular direction, and the second refers to the number of concentric circles in the mesh. The radius of the cylinder is $r_1 = 0.5$, the domain is bounded by $r_{129} = 40$, and the radii of concentric circles for 256×129 mesh are set up as
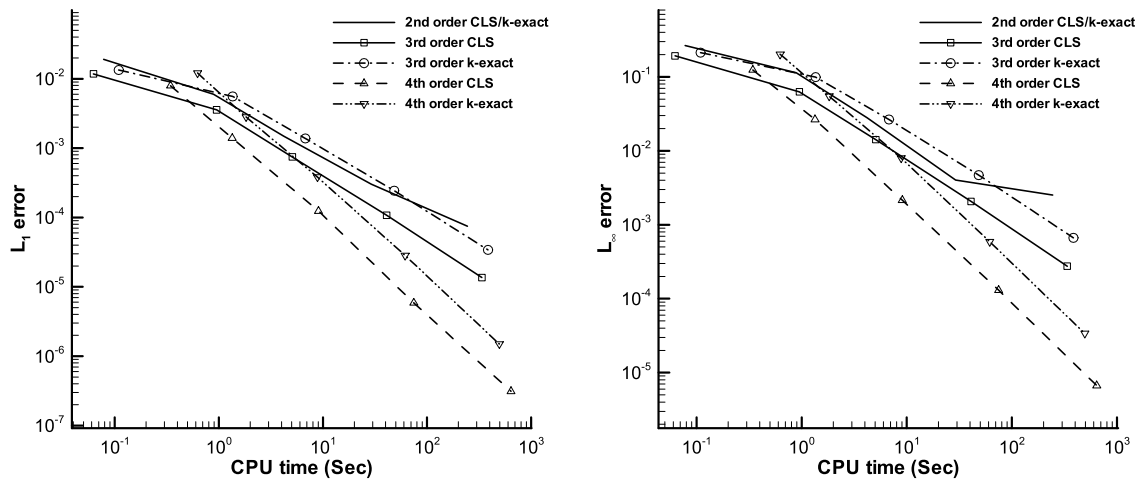
Fig. 15. Efficiency comparison for the isentropic vortex problem on irregular grids.

Table 5
CPU time and error for isentropic vortex problem on the $h = 1/4$ irregular mesh.

Schemes	Explicit TVD Runge–Kutta		Implicit Runge–Kutta (SDIRK)	
	4th order CLS	4th order k-exact	4th order CLS	4th order k-exact
CPU time (s)	43.13	9.24	9.06	8.99
L_1 error	1.38E−04	3.83E−04	1.24E−04	3.83E−004
L_∞ error	2.48E−03	7.96E−03	2.15E−03	7.95E−003

Table 6
Accuracy test results for the subsonic cylinder problem.

Schemes	Mesh	L_1 error	Order	L_2 error	Order
3rd order CLSFV	16×9	2.62E−02		4.39E−02	
	32×17	2.53E−03	3.37	7.90E−03	2.47
	64×33	3.75E−04	2.76	1.43E−03	2.46
	128×65	5.27E−05	2.83	2.58E−04	2.47
	256×129	7.31E−06	2.85	4.72E−05	2.45
4th order CLSFV	16×9	4.39E−02		7.74E−02	
	32×17	1.27E−03	5.11	5.10E−03	3.92
	64×33	8.78E−05	3.86	4.79E−04	3.41
	128×65	5.68E−06	3.95	3.79E−05	3.66
	256×129	3.73E−07	3.93	3.04E−06	3.64

$$r_i = r_1 \left(1 + \frac{2\pi}{256} \sum_{j=1}^{i-1} \alpha^j \right), \quad i = 2, \ldots, 129,$$

where $\alpha = 1.03803945$. The coarser grids are generated by successively un-refining the finest mesh.

The CFL number for the local pseudo time step is 40. The Mach number contours obtained using the third and fourth order CLSFV schemes on 64×33 grids are shown in Fig. 17. One can see that the solution obtained by the third order CLSFV scheme is more dissipative than that obtained by the fourth order CLSFV scheme. To test the accuracy of the CLSFV schemes, the entropy error defined by

$$\varepsilon_{ent} = \frac{p/p_\infty}{(\rho/\rho_\infty)^\gamma} - 1$$

is served as the error measurement. The L_1 and L_2 errors and the rates of convergence are listed in Table 6. The accuracy comparison is shown in Fig. 18. The results in Fig. 18 show that, in terms of the L_1 error, both the third and fourth order CLSFV schemes can achieve their theoretical order of accuracy; in terms of the L_2 error, the fourth order CLSFV scheme can achieve the expected fourth order while the third order CLSFV scheme shows a rate of convergence slightly lower than third order, which may be caused by the reduce of the order of reconstruction polynomial at the boundary.

To investigate the importance of the curved boundary treatment, the accuracy test results of the fourth order CLSFV scheme with straight line boundary approximation are listed in Table 7 to compare with those of the fourth order CLSFV scheme with curved boundary treatment presented in Table 6. It shows that the straight line boundary approximation
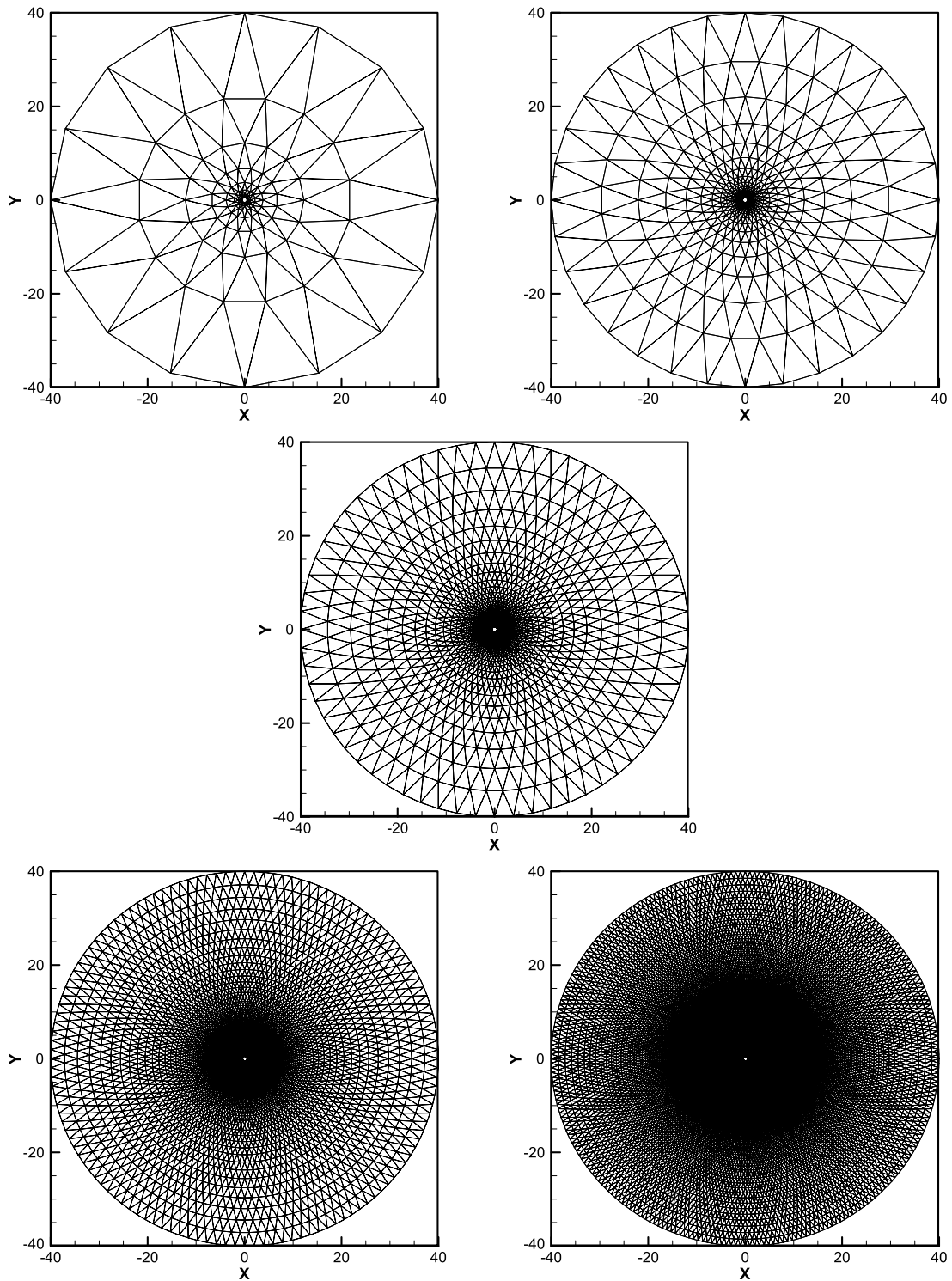
Fig. 16. Sequences of five successively globally refined meshes 16 × 9, 32 × 17, 64 × 33, 128 × 65, 256 × 129 for computing subsonic flow past a circular cylinder.

generates larger entropy error and degrades the order of accuracy of the CLSFV scheme, which demonstrates the importance of the curved boundary treatment.

Highly stretched grids are widely used in simulations of viscous flow problems. Therefore, it is necessary to verify whether the high order CLSFV method can handle this kind of grids. Four successively refined O-type grids constructed in
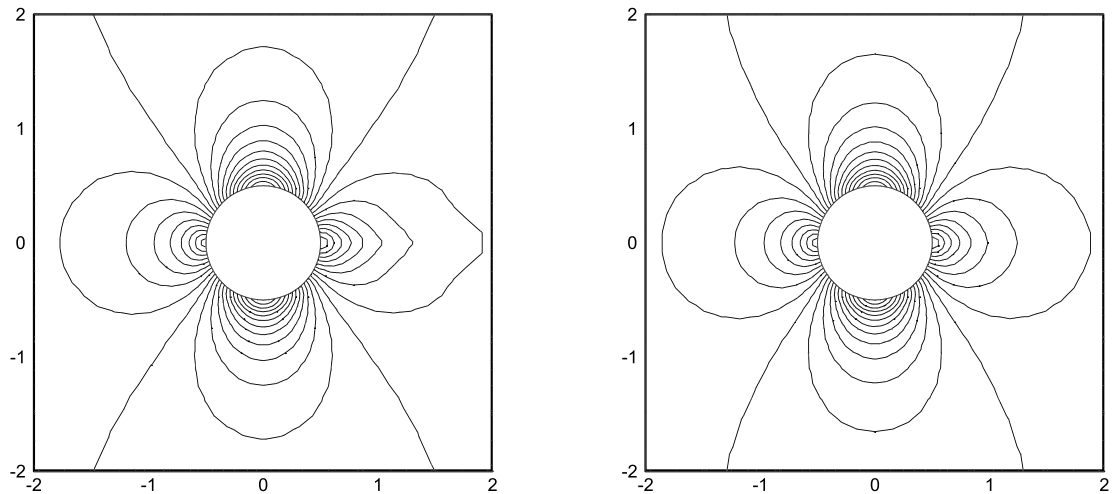
Fig. 17. Computed Mach number contours obtained by the third order (left) and forth order (right) CLSFV schemes on 64 × 33 grids.
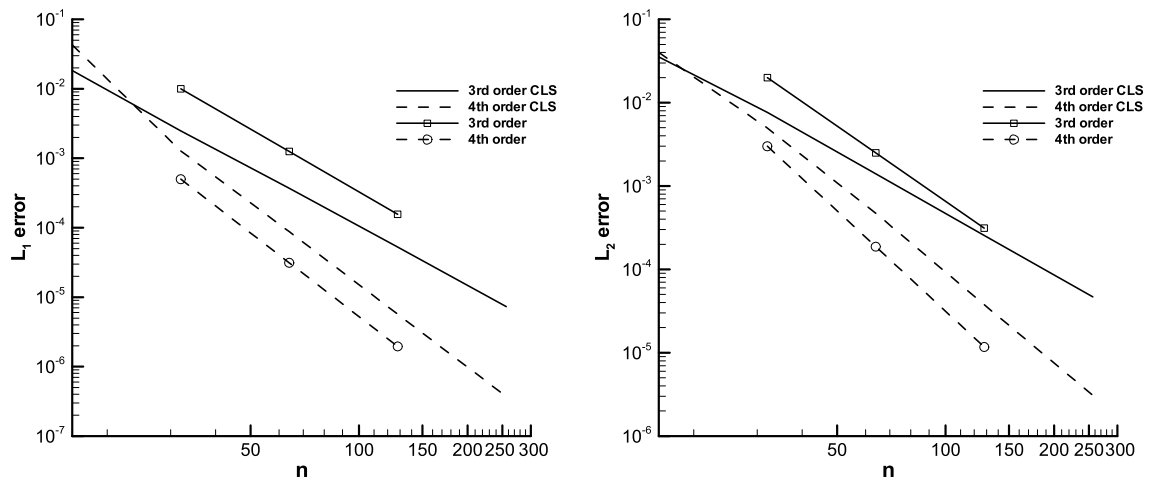
Fig. 18. Accuracy comparison for the subsonic cylinder problem.

Table 7
Accuracy test results of the fourth order CLSFV scheme using straight line boundary treatment for the subsonic cylinder problem.

Schemes	Mesh	L_1 error	Order	L_2 error	Order
4th order CLSFV with	16 × 9	5.52E−02		9.70E−02	
straight line boundary	32 × 17	1.65E−03	5.07	6.82E−03	3.83
	64 × 33	2.13E−04	2.95	1.12E−03	2.61
	128 × 65	3.99E−05	2.42	2.82E−04	1.99
	256 × 129	8.95E−06	2.16	9.63E−05	1.55

a similar way as the grids in Fig. 16 are used in the computation. The grids consist of 32 × 17, 64 × 33, 128 × 65 and 256 × 129 grid points. The radii of concentric circles for 256 × 129 mesh are set up as

$$r_i = r_1 \left(1 + \frac{1}{\beta} \frac{2\pi}{256} \sum_{j=0}^{i-2} \alpha^j \right), \quad i = 2, \ldots, 129,$$

where $\alpha = 1.06103686$ and β is the ratio of stretch for the curved elements near the wall boundary. In this paper, we choose $\beta = 10$ (the use of larger β will result in the intersection of the grid lines with the curved boundary). The 32 × 17 mesh is shown in Fig. 19 for illustration.

The accuracy test results are list in Table 8. Compared with the results in Table 6, the entropy error on the stretched grids are smaller since the stretched grids have more elements near the wall boundary. However, the order of accuracy of the CLSFV scheme on the stretched grids are slightly lower than that on the regular grids due to the low quality of mesh.
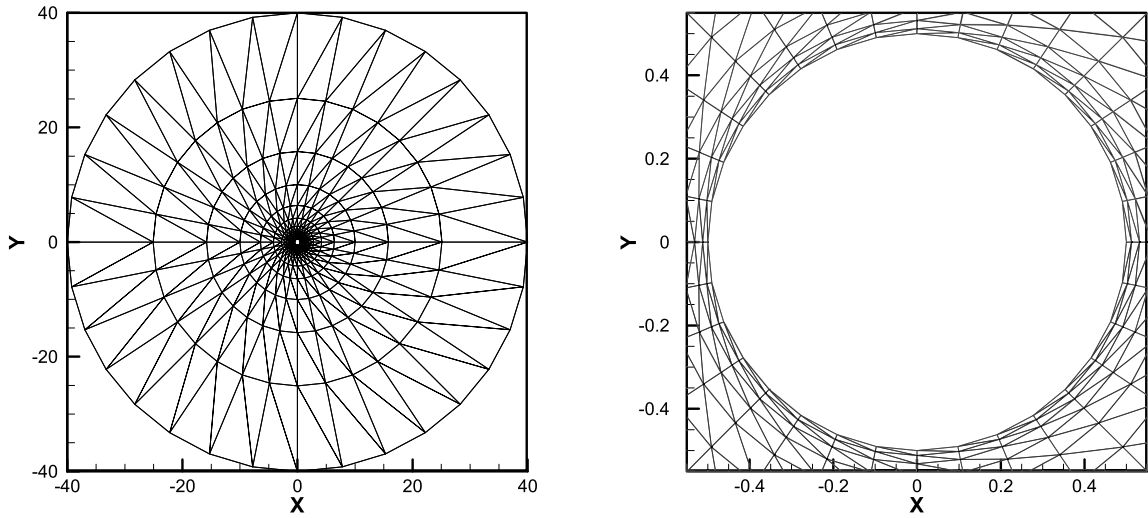
Fig. 19. Highly stretched 32×17 mesh for computing subsonic flow past a circular cylinder.

Table 8
Accuracy test results of the fourth order CLSFV scheme for the subsonic cylinder problem on stretched grids.

Schemes	Mesh	L_1 error	Order	L_2 error	Order
4th order CLSFV on stretched grids	32×17	9.90E−04		2.98E−03	
	64×33	5.65E−05	4.13	2.59E−04	3.53
	128×65	4.48E−06	3.66	2.57E−05	3.33
	256×129	3.71E−07	3.59	2.68E−06	3.26
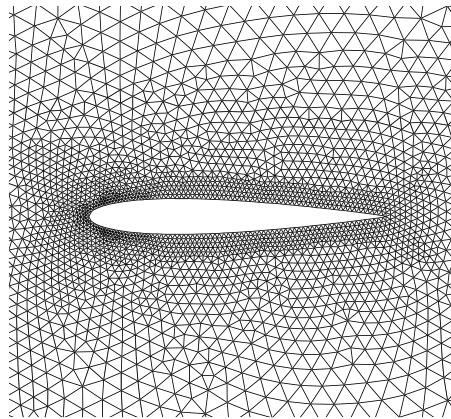
Fig. 20. Unstructured mesh (nelem = 10 382, npoint = 5306, nbound = 150) used for computing subsonic flow past a NACA0012 airfoil.

3.3. Subsonic flow around NACA0012 airfoil

This problem is used to test the convergence performance of the high order CLSFV schemes for steady flow simulation. The k-exact FV schemes are also tested to compare with the CLSFV schemes. The unstructured mesh used in the simulation is shown in Fig. 20, which consists of 10 382 elements, 5306 grid points and 150 boundary points.

The far field condition of test case is the Mach 0.3 subsonic inflow at the angle of $1.25°$. We compute this test case with the second, third and fourth order CLSFV and k-exact FV schemes. All computations are started with uniform flow. The CFL number for the local pseudo time step is 40. The comparison of convergence histories is shown in Fig. 21. The results in Fig. 21 show that all the schemes can converge to machine zero, which demonstrates the superior convergence property of these schemes. Schemes of the same order of accuracy use almost the same CPU time to reach steady-state solution. To compare the computational efficiency of the CLSFV and k-exact FV schemes, we show the comparison of the convergence histories in terms of the L_1 and L_∞ norms of the entropy error in Fig. 22. It can be seen clearly that the CLSFV schemes can obtain much more accurate solutions than that of the k-exact FV schemes using nearly the same CPU time, which indicates
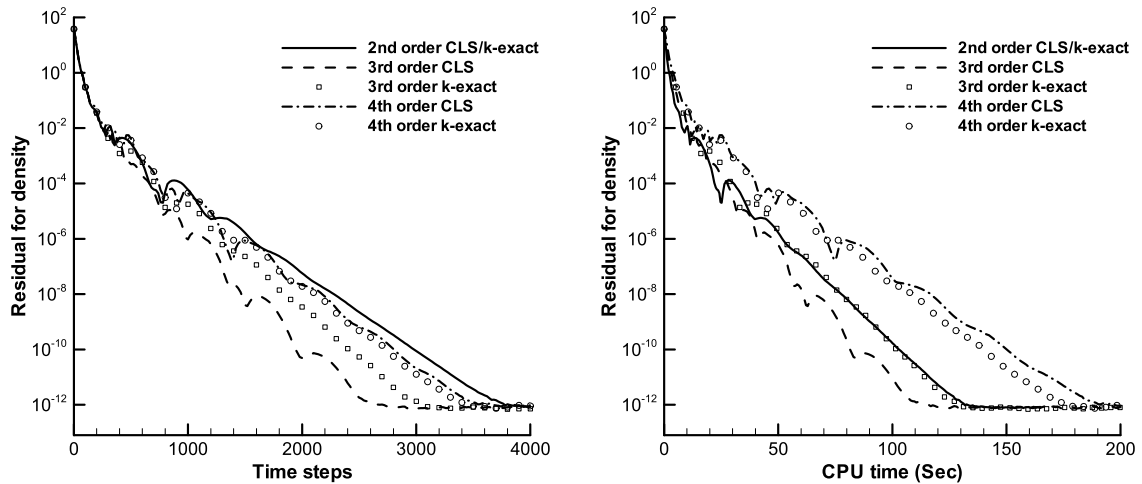
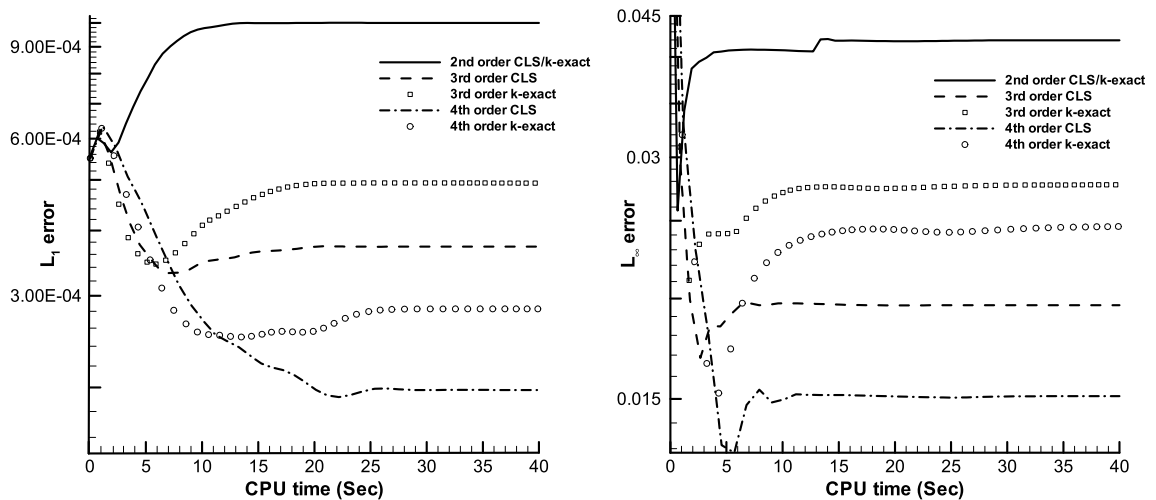Fig. 21. Convergence history comparison for subsonic flow past a NACA0012 airfoil problem.

Fig. 22. Entropy error comparison for subsonic flow past a NACA0012 airfoil problem.

that the CLSFV schemes are more efficient than the k-exact FV schemes. Furthermore, the results in Fig. 21 and Fig. 22 show that, the high order FV schemes are much more efficient than the second order FV scheme.

3.4. Double Mach reflection problem

The double Mach reflection problem [54] is a popular test case for high-resolution schemes. The whole computational domain is $[0, 4] \times [0, 1]$. The wall is located at the bottom of the computational domain beginning at $x = 1/6$. Initially, a right-moving shock with $Ma = 10$ is located at $x = 1/6$, $y = 0$, inclined $60°$ with respect to the x-axis. The computations are performed until $t = 0.2$.

The computations are performed on a mesh with grid size $h = 1/240$ using a physical time step $\Delta t = 0.0002$. The CFL number for the local pseudo time step is 10 and the convergence criterion for the inner iteration is $\varepsilon = 10^{-3}$. The computed density contours are shown in Figs. 23 and 24. From these figures we can clearly see that all the numerical results are basically oscillation-free and the higher order schemes capture the complicated flow structures near the Mach stem much better than the lower order schemes. Furthermore, the CLSFV schemes give better resolutions for the shear layer and the vortex which is developed from the shock triple point and the Mach stem than the k-exact FV schemes, which demonstrate the high-resolution property of the CLSFV method.

Table 9 gives the CPU time comparison between the four schemes. The third order CLSFV scheme uses 10.5% more CPU time than the third order k-exact FV scheme and fourth order CLSFV scheme uses 29.0% more CPU time than the fourth order k-exact FV scheme.

(a) 3rd order CLSFV

(b) 3rd order k-exact FV

(c) 4th order CLSFV

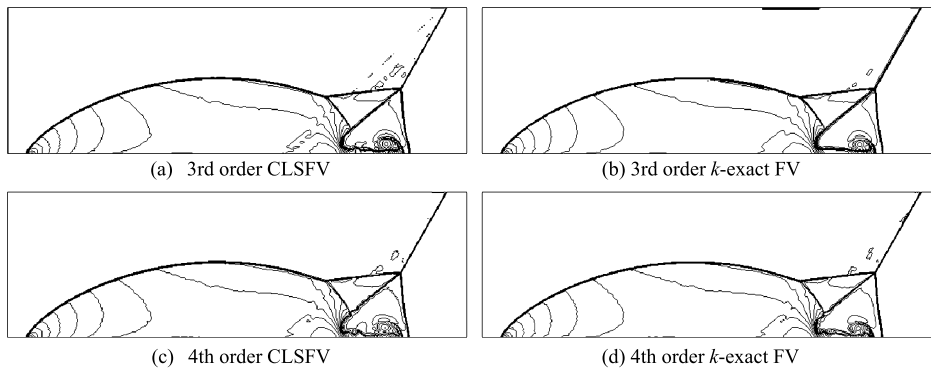(d) 4th order k-exact FV

Fig. 23. Comparison of density contours for double Mach reflection on grids with size $h = 1/240$. Thirty equally spaced contour lines between 2.05 and 21.31.
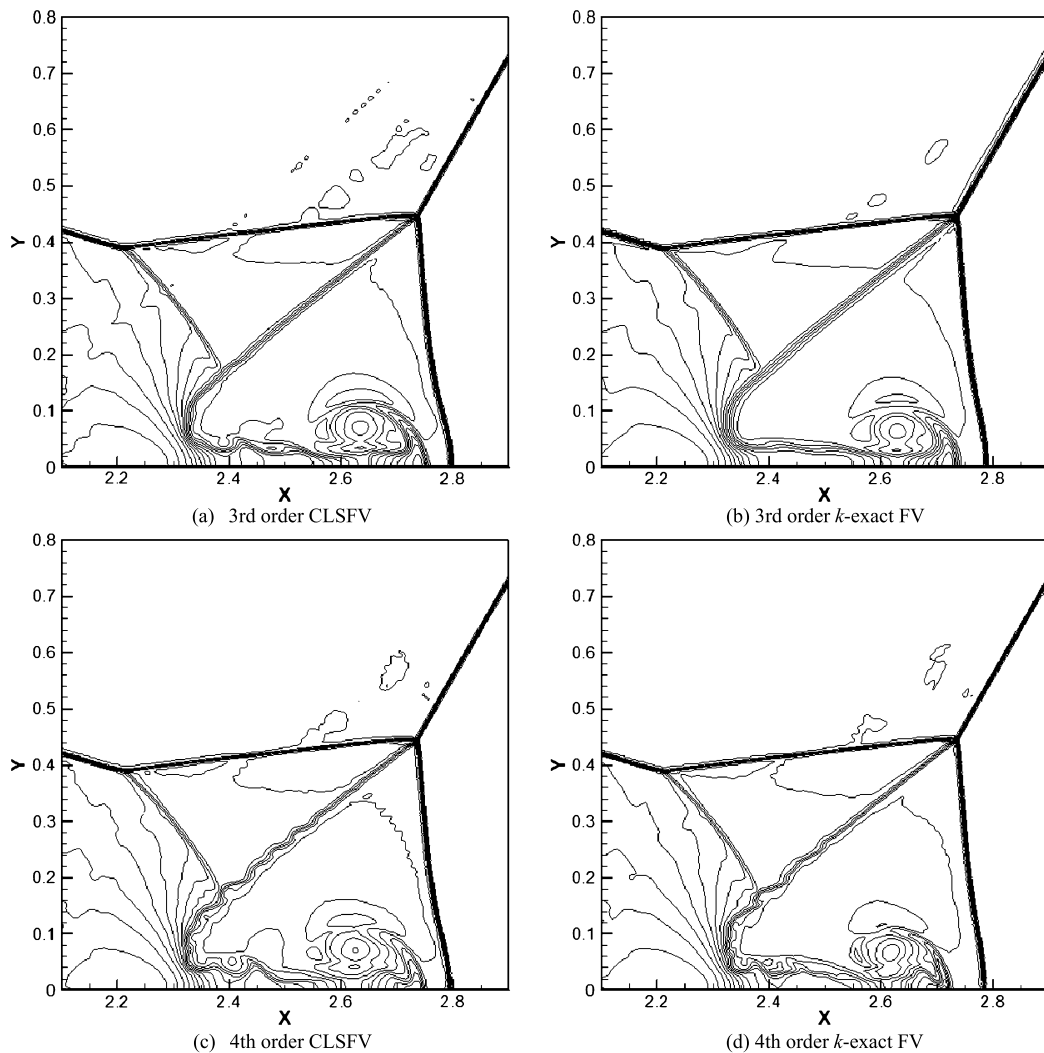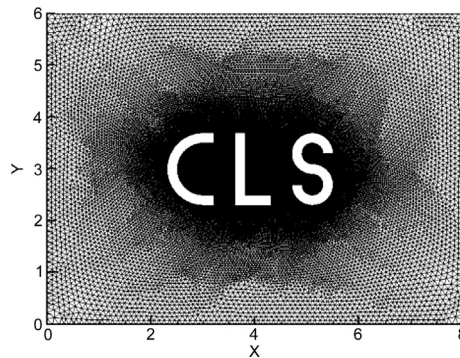

(a) 3rd order CLSFV

(b) 3rd order k-exact FV

(c) 4th order CLSFV

(d) 4th order k-exact FV

Fig. 24. Close-up view around the double Mach stem of Fig. 23.

Table 9
CPU time comparison for the double Mach reflection problem.

Schemes	3rd order CLS	3rd order k-exact	4th order CLS	4th order k-exact
CPU time (s)	30 619.05	27 701.07	45 722.75	35 440.90

Fig. 25. Unstructured mesh (nelem = 157 124, npoint = 79 685, nbound = 1971) used for computing Mach 2 shock wave past complex shape obstacles.
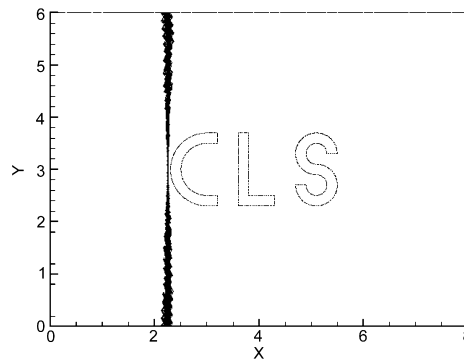
Fig. 26. Density contours at $t = 0$ for the Mach 2 shock wave past complex shape obstacles problem. Thirty equally spaced contour lines between 1.48 and 3.66.

3.5. A Mach 2 shock wave past complex shape obstacles

This test case is used to verify the CLSFV method's capability of handling both complex physics and geometries. The computational domain is $[0, 8] \times [0, 6]$. Initially, a right-moving shock with $Ma = 2$ is located at $x = 2.25$, perpendicular to the x-axis, which is shown in Fig. 26. The initial conditions are presented in detail as follows

$$(\rho_0, u_0, v_0, p_0) = \begin{cases} (3.73324, 1.24998, 0, 4.5) & \text{for } 0 \leq x < 2.25 \\ (1.4, 0, 0, 1) & \text{for } 2.25 \leq x \leq 10 \end{cases}$$

The mesh used in this computation is shown in Fig. 25, which consists of 157 124 elements, 79 685 grid points and 1971 boundary points. The computations are performed until $t = 2.5$ using a physical time step $\Delta t = 0.001$. The CFL number for the local pseudo time step is 10 and the convergence criterion for the inner iteration is $\varepsilon = 10^{-3}$.

The density contours at $t = 0.5, 1.0, 1.5, 2.0, 2.5$ computed by the third and fourth order CLSFV schemes are presented in Figs. 27–31. From these figures we can see that the high order CLSFV schemes can obtain basically oscillation-free solutions and resolve important flow features. The density contours around the obstacles at $t = 1.5$ in Fig. 32 are used to show the complexity of the flow structures. The results demonstrate the schemes' capability of handling both complex physics and geometries.

4. Conclusions

The CLSFV method is successfully extended to two-dimensional Euler equations. In the multi-dimensional CLS reconstruction, a set of constitutive relations are constructed by requiring the reconstruction polynomial and its spatial derivatives on the control volume of interest to conserve their averages on the face-neighboring cells. These relations result in an over-determined system of linear equations, which, in the sense of least-squares, corresponds to a large sparse linear equation system that needs to be solved iteratively. An implicit reconstruction and implicit time integration coupled iteration
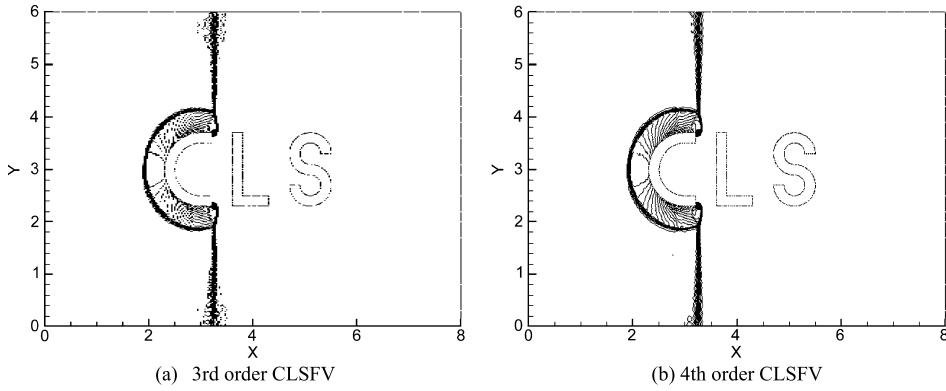
Fig. 27. Density contours at $t = 0.5$ for the Mach 2 shock wave past complex shape obstacles problem. Thirty equally spaced contour lines between 1.00 and 6.74.
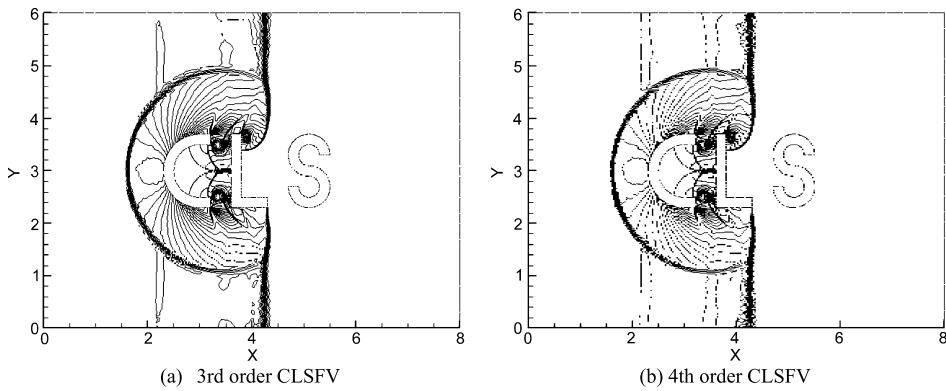

Fig. 28. Density contours at $t = 1.0$ for the Mach 2 shock wave past complex shape obstacles problem. Thirty equally spaced contour lines between 0.52 and 6.31.
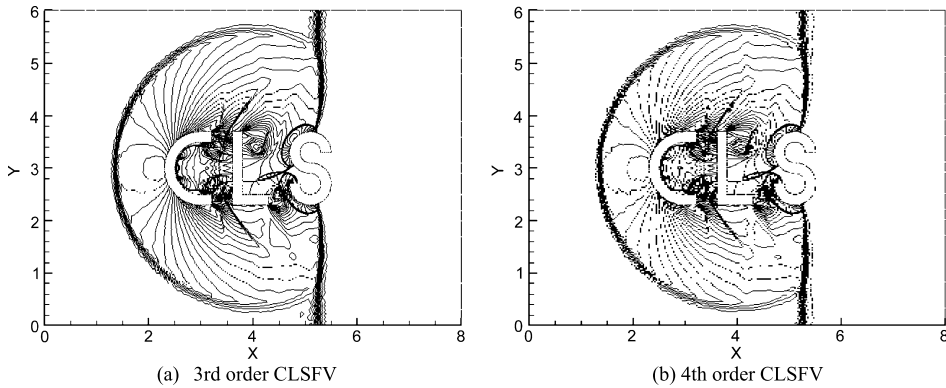

Fig. 29. Density contours at $t = 1.5$ for the Mach 2 shock wave past complex shape obstacles problem. Thirty equally spaced contour lines between 0.43 and 6.11.

method is developed to avoid deterioration of the computational efficiency. The problem-independent shock detector and the WBAP limiter are used to efficiently suppress non-physical oscillations in the vicinity of discontinuities. Numerical results demonstrate the high order accuracy, high computational efficiency and capability of handling both complex physics and geometries of the proposed method.

Acknowledgements

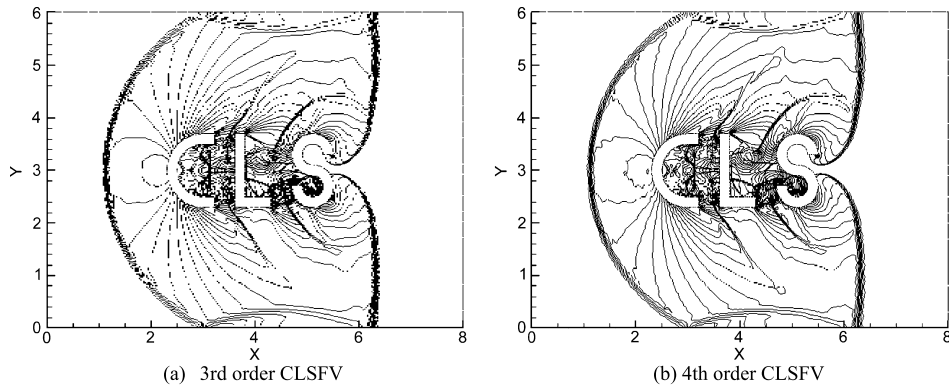(a) 3rd order CLSFV   (b) 4th order CLSFV

Fig. 30. Density contours at $t = 2.0$ for the Mach 2 shock wave past complex shape obstacles problem. Thirty equally spaced contour lines between 0.54 and 7.98.

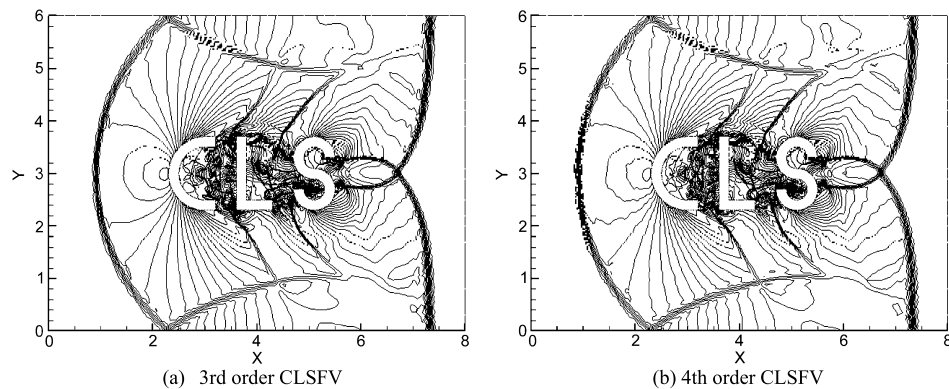(a) 3rd order CLSFV   (b) 4th order CLSFV

Fig. 31. Density contours at $t = 2.5$ for the Mach 2 shock wave past complex shape obstacles problem. Thirty equally spaced contour lines between 0.30 and 6.27.
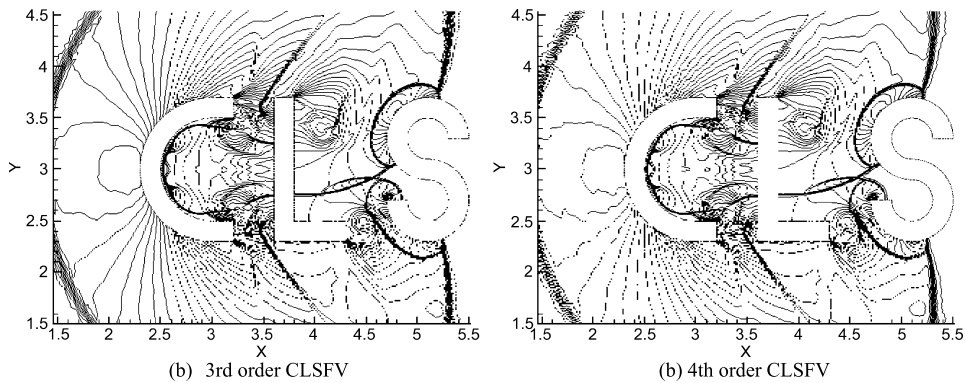

(b) 3rd order CLSFV   (b) 4th order CLSFV

Fig. 32. Close-up view around the obstacles of Fig. 29.

References

[1] Q. Wang, Y.X. Ren, W. Li, Compact high order finite volume method on unstructured grids I: basic formulations and one-dimensional schemes, J. Comput. Phys. (2016), http://dx.doi.org/10.1016/j.jcp.2016.01.036.

[2] W.H. Reed, T.R. Hill, Triangular mesh methods for the neutron transport equation, Los Alamos Report LA-UR-73-479, 1973.

[3] B. Cockburn, C.W. Shu, TVB Runge–Kutta local projection discontinuous Galerkin finite element method for conservation laws. II. General framework, Math. Comput. 52 (186) (1989) 411–435.

[4] B. Cockburn, S.Y. Lin, C.W. Shu, TVB Runge–Kutta local projection discontinuous Galerkin finite element method for conservation laws III: one-dimensional systems, J. Comput. Phys. 84 (1) (1989) 90–113.

[5] B. Cockburn, S. Hou, C.W. Shu, The Runge–Kutta local projection discontinuous Galerkin finite element method for conservation laws. IV. The multidimensional case, Math. Comput. 54 (190) (1990) 545–581.

[6] B. Cockburn, C.W. Shu, Runge–Kutta discontinuous Galerkin methods for convection-dominated problems, J. Sci. Comput. 16 (3) (2001) 173–261.

[7] M. Dumbser, D.S. Balsara, E.F. Toro, C.D. Munz, A unified framework for the construction of one-step finite volume and discontinuous Galerkin schemes on unstructured meshes, J. Comput. Phys. 227 (18) (2008) 8209–8253.

[8] M. Dumbser, Arbitrary high order P_NP_M schemes on unstructured meshes for the compressible Navier–Stokes equations, Comput. Fluids 39 (1) (2010) 60–76.

[9] M. Dumbser, O. Zanotti, Very high order P_NP_M schemes on unstructured meshes for the resistive relativistic MHD equations, J. Comput. Phys. 228 (18) (2009) 6991–7006.

[10] H. Luo, L. Luo, R. Nourgaliev, V.A. Mousseau, N. Dinh, A reconstructed discontinuous Galerkin method for the compressible Navier–Stokes equations on arbitrary grids, J. Comput. Phys. 229 (19) (2010) 6961–6978.

[11] L. Zhang, W. Liu, L. He, X. Deng, H. Zhang, A class of hybrid DG/FV methods for conservation laws I: basic formulation and one-dimensional systems, J. Comput. Phys. 231 (4) (2012) 1081–1103.

[12] L. Zhang, W. Liu, L. He, X. Deng, H. Zhang, A class of hybrid DG/FV methods for conservation laws II: two-dimensional cases, J. Comput. Phys. 231 (4) (2012) 1104–1120.

[13] R. Abgrall, M. Mezine, Construction of second order accurate monotone and stable residual distribution schemes for unsteady flow problems, J. Comput. Phys. 188 (1) (2003) 16–55.

[14] M. Ricchiuto, Á. Csík, H. Deconinck, Residual distribution for general time-dependent conservation laws, J. Comput. Phys. 209 (1) (2005) 249–289.

[15] R. Abgrall, Residual distribution schemes: current status and future trends, Comput. Fluids 35 (7) (2006) 641–669.

[16] R. Abgrall, A. Larat, M. Ricchiuto, Construction of very high order residual distribution schemes for steady inviscid flow problems on hybrid unstructured meshes, J. Comput. Phys. 230 (11) (2011) 4103–4136.

[17] Z.J. Wang, Spectral (finite) volume method for conservation laws on unstructured grids: basic formulation, J. Comput. Phys. 178 (1) (2002) 210–251.

[18] Z.J. Wang, Y. Liu, Spectral (finite) volume method for conservation laws on unstructured grids II: extension to two-dimensional scalar equation, J. Comput. Phys. 179 (2) (2002) 665–697.

[19] Z.J. Wang, Y. Liu, Spectral (finite) volume method for conservation laws on unstructured grids III: one dimensional systems and partition optimization, J. Sci. Comput. 20 (1) (2004) 137–157.

[20] Z.J. Wang, L. Zhang, Y. Liu, Spectral (finite) volume method for conservation laws on unstructured grids IV: extension to two-dimensional systems, J. Comput. Phys. 194 (2) (2004) 716–741.

[21] Y. Liu, M. Vinokur, Z.J. Wang, Spectral difference method for unstructured grids I: basic formulation, J. Comput. Phys. 216 (2) (2006) 780–801.

[22] Z.J. Wang, Y. Liu, G. May, A. Jameson, Spectral difference method for unstructured grids II: extension to the Euler equations, J. Sci. Comput. 32 (1) (2007) 45–71.

[23] G. May, A. Jameson, A spectral difference method for the Euler and Navier–Stokes equations on unstructured meshes, AIAA paper 2006-304, 2006.

[24] Z.J. Wang, H. Gao, A unifying lifting collocation penalty formulation including the discontinuous Galerkin, spectral volume/difference methods for conservation laws on mixed grids, J. Comput. Phys. 228 (21) (2009) 8161–8186.

[25] H.T. Huynh, A flux reconstruction approach to high-order schemes including discontinuous Galerkin methods, AIAA paper 2007-4079, 2007.

[26] T.J. Barth, P.O. Frederickson, Higher order solution of the Euler equations on unstructured grids using quadratic reconstruction, AIAA paper 90-0013, 1990.

[27] M. Delanaye, Y. Liu, Quadratic reconstruction finite volume schemes on 3D arbitrary unstructured polyhedral grids, AIAA paper 99-3259, 1999.

[28] C. Ollivier-Gooch, M. Van Altena, A high-order-accurate unstructured mesh finite-volume scheme for the advection–diffusion equation, J. Comput. Phys. 181 (2) (2002) 729–752.

[29] C.F. Ollivier-Gooch, Quasi-ENO schemes for unstructured meshes based on unlimited data-dependent least-squares reconstruction, J. Comput. Phys. 133 (1) (1997) 6–17.

[30] O. Friedrich, Weighted essentially non-oscillatory schemes for the interpolation of mean values on unstructured grids, J. Comput. Phys. 144 (1) (1998) 194–212.

[31] M. Dumbser, M. Käser, Arbitrary high order non-oscillatory finite volume schemes on unstructured meshes for linear hyperbolic systems, J. Comput. Phys. 221 (2) (2007) 693–723.

[32] M. Dumbser, M. Käser, V.A. Titarev, E.F. Toro, Quadrature-free non-oscillatory finite volume schemes on unstructured meshes for nonlinear hyperbolic systems, J. Comput. Phys. 226 (1) (2007) 204–243.

[33] C. Hu, C.W. Shu, Weighted essentially non-oscillatory schemes on triangular meshes, J. Comput. Phys. 150 (1) (1999) 97–127.

[34] J.M.C. Pereira, M.H. Kobayashi, J.C.F. Pereira, A fourth-order-accurate finite volume compact method for the incompressible Navier–Stokes solutions, J. Comput. Phys. 167 (1) (2001) 217–243.

[35] C. Lacor, S. Smirnov, M. Baelmans, A finite volume formulation of compact central schemes on arbitrary structured grids, J. Comput. Phys. 198 (2) (2004) 535–566.

[36] A. Fosso, H. Deniau, F. Sicot, P. Sagaut, Curvilinear finite-volume schemes using high-order compact interpolation, J. Comput. Phys. 229 (13) (2010) 5090–5122.

[37] P.L. Roe, Approximate Riemann solvers, parameter vectors, and difference schemes, J. Comput. Phys. 43 (2) (1981) 357–372.

[38] R. Sanders, E. Morano, M.C. Druguet, Multidimensional dissipation for upwind schemes: stability and applications to gas dynamics, J. Comput. Phys. 145 (2) (1998) 511–537.

[39] R. Abgrall, On essentially non-oscillatory schemes on unstructured meshes: analysis and implementation, J. Comput. Phys. 114 (1) (1994) 45–58.

[40] W. Li, Y.X. Ren, The multi-dimensional limiters for solving hyperbolic conservation laws on unstructured grids II: extension to high order finite volume schemes, J. Comput. Phys. 231 (11) (2012) 4053–4077.

[41] B. Gustafsson, The convergence rate for difference approximations to mixed initial boundary value problems, Math. Comput. 29 (130) (1975) 396–406.

[42] W. Li, Efficient Implementation of High-Order Accurate Numerical Methods on Unstructured Grids, Springer, 2014.

[43] W. Li, Y.X. Ren, G. Lei, H. Luo, The multi-dimensional limiters for solving hyperbolic conservation laws on unstructured grids, J. Comput. Phys. 230 (21) (2011) 7775–7795.

[44] W. Li, Y.X. Ren, High-order k-exact WENO finite volume schemes for solving gas dynamic Euler equations on unstructured grids, Int. J. Numer. Methods Fluids 70 (6) (2012) 742–763.

[45] A. Arnone, M.S. Liou, L.A. Povinelli, Integration of Navier–Stokes equations using dual time stepping and a multigrid method, AIAA J. 33 (6) (1995) 985–990.

[46] L.P. Zhang, Z.J. Wang, A block LU-SGS implicit dual time-stepping algorithm for hybrid dynamic meshes, Comput. Fluids 33 (7) (2004) 891–916.

[47] L. Ferracina, M.N. Spijker, Strong stability of singly-diagonally-implicit Runge–Kutta methods, Appl. Numer. Math. 58 (11) (2008) 1675–1686.

[48] H. Luo, J.D. Baum, R. Löhner, A fast, matrix-free implicit method for compressible flows on unstructured grids, J. Comput. Phys. 146 (2) (1998) 664–690.

[49] X. Zhong, Additive semi-implicit Runge–Kutta methods for computing high-speed nonequilibrium reactive flows, J. Comput. Phys. 128 (1) (1996) 19–31.

[50] M.P. Martín, G.V. Candler, A parallel implicit method for the direct numerical simulation of wall-bounded compressible turbulence, J. Comput. Phys. 215 (1) (2006) 153–171.

[51] C. Hu, C.W. Shu, Weighted essentially non-oscillatory schemes on triangular meshes, J. Comput. Phys. 150 (1) (1999) 97–127.

[52] C.W. Shu, S. Osher, Efficient implementation of essentially non-oscillatory shock-capturing schemes, J. Comput. Phys. 77 (2) (1988) 439–471.
[53] H. Luo, J.D. Baum, R. Löhner, A Hermite WENO-based limiter for discontinuous Galerkin method on unstructured grids, J. Comput. Phys. 225 (1) (2007) 686–713.
[54] P. Woodward, P. Colella, The numerical simulation of two-dimensional fluid flow with strong shocks, J. Comput. Phys. 54 (1) (1984) 115–173.